Breakup of Liquid Feedstock in Plasma Spraying

Saman Shalbaf

A Thesis
in
The Department
of
Mechanical, Industrial and Aerospace Engineering (MIAE)

Presented in Partial Fulfillment of the Requirements
For the Degree of
Master of Applied Science (Mechanical Engineering)

at Concordia University
Montreal, Quebec, Canada

December 2021

CONCORDIA UNIVERSITY

School of Graduate Studies

This is to certify that the thesis is prepared

By: **Saman Shalbaf**

Entitled: **Breakup of Liquid Feedstock in Plasma Spraying**

and submitted in partial fulfillment of the requirements for the degree of

Master of Applied Science (Mechanical Engineering)

Complies with the regulations of this University and meets the accepted standards with respect to originality and quality.

Signed by the final examining committee:

_____ Chair
Dr. M. Paraschivoiu

_____ Examiner
Dr. M. Paraschivoiu

_____ Examiner
Dr. Attila Zsaki

_____ Thesis Supervisor
Dr. Ali Dolatabadi

Approved by _____
Dr. Martin Pugh, Chair of Department

December 15, 2021

_____
Dr. Mourad Debbai, Dean of
Gina Cody School of Engineering and
Computer Science

Abstract

Breakup of Liquid Feedstock in Plasma Spraying

Saman Shalbaf

Suspension plasma spray is an emerging technology to produce functional nanostructured coatings at moderate cost. In general, in this technique, the liquid is injected radially into a high-velocity high-temperature plasma flow. After liquid breakup and evaporation, solid particles remain in the field and impact the substrate. Preliminary studies have shown that liquid jet atomization is the primary phenomenon that controls the coating quality. However, due to the complex thermophysical properties of plasma and its intricate flow physics, the breakup processes of liquid jets in plasma crossflows have not been investigated comprehensively yet. In general, the gaseous Reynolds number and the liquid-to-gas density ratio in this process are around 50 and 10,000, respectively, which are far outside the limits commonly observed in engines and wind tunnels. In this regard, detailed features of the breakup phenomena of the liquid jets injected in plasma and air crossflow are provided. Moreover, a case study has been established to analyze the effect of changing the surface tension of the liquid in the plasma spray process. The finite volume scheme is used to solve the incompressible variable-density Navier-Stokes equations. In addition, the volume of fluid (VOF) approach is utilized to track the gas-liquid interfaces. Finally, qualitative results such as instantaneous snapshots and shape of the liquid jet cross-sections, in company with quantitative data like including fracture point location, length of surface waves and size of the droplets have been presented.

Acknowledgments

I would like to, cordially and truthfully, express my gratitude to my research supervisor, Prof. Ali Dolatabadi, for his continuous patience, support and motivation. Without his guidance and comment, the completion of this dissertation would not have been possible.

Also, the financial support provided by the NSERC is truly acknowledged.

I wish to thank the great love of my wife, Reihane; my daughter, Diana; and my parents. They encouraged me from the beginning with their patience and confidence.

Finally, I would like to express my appreciation to my colleagues and friends, Dr. Mehdi Jadidi and Mr. Hooman Hashemi, for their assistance and comments in several stages of the research.

Contents

List of Figures

List of Tables

Nomenclature

C	Color function
d_0	Injector orifice diameter (m)
f	Mean value of C
f_a	Fraction of the fluid advected the cell surface
$F_{f,i}$	Volume-fraction flux (m^3/s)
$\boldsymbol{f}$	Body force vector (N/m^3)
Fr	Froude number
g	Gravity acceleration (m/s^2)
L	Length scale (m)
$\boldsymbol{n}$	Normal unit vector of the interface
Oh	Ohnesorge number
p	Flow pressure field (N/m^2)
q	Momentum flux ratio
r	Radial distance (m)
r_μ	Viscosity ratio
r_ρ	Density ratio
R	Exit radius of the plasma torch (m)
Re	Reynolds number
S	Surface area (m^2)
T	Temperature (K)
$\boldsymbol{u}$	Flow velocity field (m/s)
$u_{f,i}$	Component of the velocity at the cell surface (m/s)
U	Velocity (m/s)

We	Weber number
x	Coordinate in direction of crossflow
y	Coordinate in direction of liquid injection
z	Coordinate orthogonal to x and z
Δx	Cell size (m)
κ	Local curvature (m/s^2)
λ	Wavelength (m)
μ	Dynamic viscosity (N.s/m^2)
ρ	Density (kg/m^3)
σ	Surface tension (N/m)

Subscripts

a	Ambient property
b	Breakup location
g	Gaseous property
l	Liquid property
m	Property at the centerline of the plasma torch exit

Acronyms

AMR	Adaptive mesh refinement
APS	Atmospheric plasma spray
BCG	Bell-Collela-Glaz
KHRT	Kelvin-Helmholtz Rayleigh-Taylor
LES	Large eddy simulation
LJIC	Liquid jet in crossflow
MCVOF	Momentum-conserving volume-of-fluid
MPI	Message passing interface
MYC	Mixed-Youngs-Centered
PDF	Probability density function
PLIC	Piecewise linear interface construction
RANS	Reynolds averaged Navier-Stokes
RNG	Re-normalisation group
SGN	Serre-Green-Naghdi
SOFC	Solid oxide fuel cell
SPPS	Solution precursor plasma spraying
SPS	Suspension plasma spraying
TBC	Thermal barrier coating
VOF	Volume of fluid

Chapter 1

Introduction

1.1 Liquid Jet Atomization in Crossflow

Injection of liquid jets from an orifice into a crossflow is one of the mechanisms that is employed for the rapid mixing of two separate fluids in a small space. In other words, injecting liquid jets in transverse free air jets mixes fine droplets with the crossflow and enhances heat and mass transfer between liquid and gas phases. For example, the vaporization rate in the gas turbine engines and oil burners, is influenced strongly by the fuel atomization because of the significant increase of the total surface area of the injected fuel [1]. Moreover, the injection of Liquid Jet in Crossflow (LJIC) was motivated by the applications in diesel engines, suspension/solution thermal sprays, spark-ignition engines, and agricultural sprays, among others [2],[3]. This variety of applications mentions the role of understanding the atomization mechanism of the LJIC from the onset to the end of the process.

The breakup of a liquid jet injected in a crossflow involves two serial processes. The process by which a column of liquid initially breaks into ligaments and droplets is named ‘‘primary breakup’’. Then, the primary drops which were formed via the primary breakup can undergo ‘‘secondary breakup’’ and lead to smaller droplets and, ultimately, the formation of the desired spray in the far-field region [4]. One should consider these different breakup mechanisms to comprehend the fundamental characteristics of the LJIC phenomenon.

Fig.1.1 shows a schematic description of a round liquid jet penetrating transversely into a gaseous crossflow while the breakup process of the jet is illustrated. While emerging the liquid jet from the injector, the aerodynamic forces bend the jet column toward the crossflow direction. Moreover, the jet column deforms from a circular cross-section to an ellipsoidal one. Likewise, a stagnation point occurs in the crossflow on the windward side of the column, while the leeward side hosts a low-pressure zone.

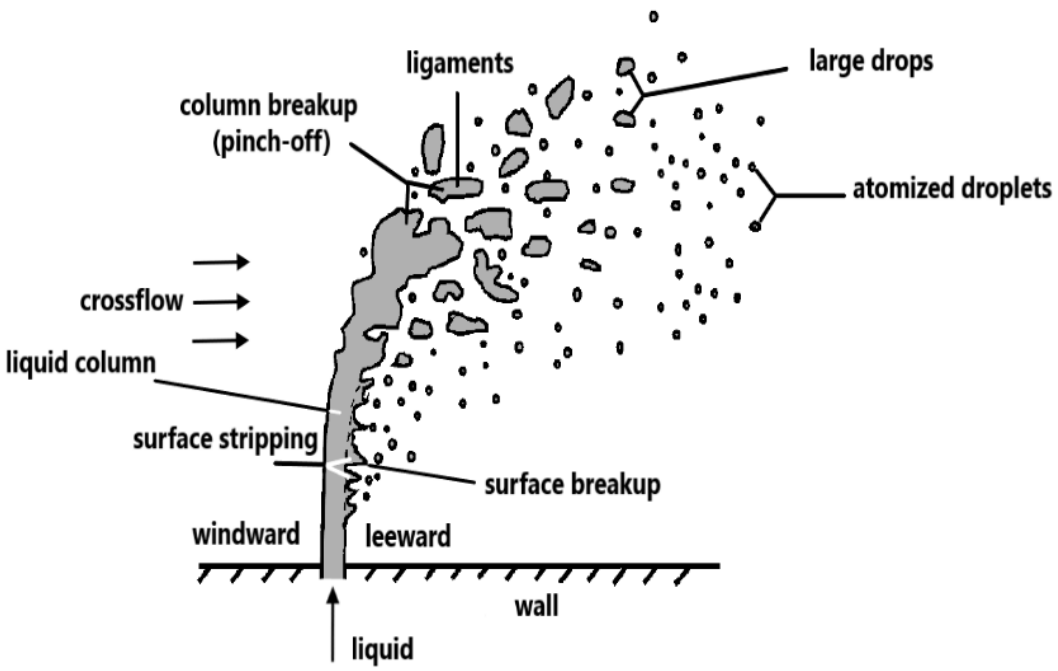

Figure 1.1: Visualization of breakup process of a round liquid jet in gaseous crossflow, adapted from [5].

On the windward side of the liquid jet, "column" or "capillary" waves start appearing and break the liquid column into ligaments and later to droplets [6]. This breakup mechanism is called column breakup. Simultaneously, the gas flow passes the stagnation point and accelerates as it flows around to the sides of the column. This flow develops transverse surface waves [7]. These "surface" and "aerodynamic" waves break the jet into ligaments by stripping the droplets from the leeward surface. This pinch-off process is called surface stripping or surface breakup.

Comprehending the role of the features that affect the breakup mechanism can help to control the final droplet size distribution to get more profound knowledge about the fundamentals of the processes mentioned above. Amongst these features, nozzle internal flow, material properties of the two fluids, jet surface waves, velocity profile at the atomizer exit, crossflow velocity magnitude and direction, and turbulence at the nozzle exit are mentionable.

Correspondingly, four forces act on the liquid jet: inertia, $\rho L^2 U^2$; surface tension force, σL; viscous force, μLU; and gravity force, $\rho L^3 g$; where L, U, g, ρ, σ, and μ represent the characteristic length of the jet (i.e. jet diameter), mean axial jet velocity, gravity acceleration, density, surface tension, and dynamic viscosity, respectively. The instability waves imposed by these forces on the liquid jet core are the main reason for jet fragmentation. To address these forces, four non-dimensional numbers: Reynolds number, $Re = \frac{\rho LU}{\mu}$; Weber number, $We = \frac{\rho LU^2}{\sigma}$; Froude number, $Fr = \frac{U^2}{gL}$; and Ohnesorge number, $Oh = \frac{We^{0.5}}{Re}$ are defined [8]. In this study, the primary controlling parameters include crossflow Reynolds number $Re_g = \rho_g u_g d_0/\mu_g$, density ratio $r_\rho = \rho_l/\rho_g$, gaseous Weber number $We_g = \rho_g u_g^2 d_0/\sigma$, momentum flux ratio $q = \rho_l u_l^2/\rho_g u_g^2$ and the viscosity ratio $r_\mu = \mu_l/\mu_g$.

1.2 Suspension Plasma Spray Process

Atomization of liquid jets in a crossflowing stream is of great interest to the thermal spray processes. In these processes, molten, semi-molten, or solid coating particles are deposited on the substrate after being heated and accelerated by a high-temperature high-velocity jet or flame [9]. One of the advantages of thermal spray processes is using various materials to produce different coatings to enhance components' ability to resist corrosion, wear, or high temperatures [10],[11].

There are different thermal spray processes, depending on the feedstock materials and heat sources. Among them, thermal plasma spraying is one of the most favorable techniques in synthesizing coatings and structural components of improved properties and is widely implemented in research laboratories and industry. Fig.1.2 shows a schematic of the plasma spray process.

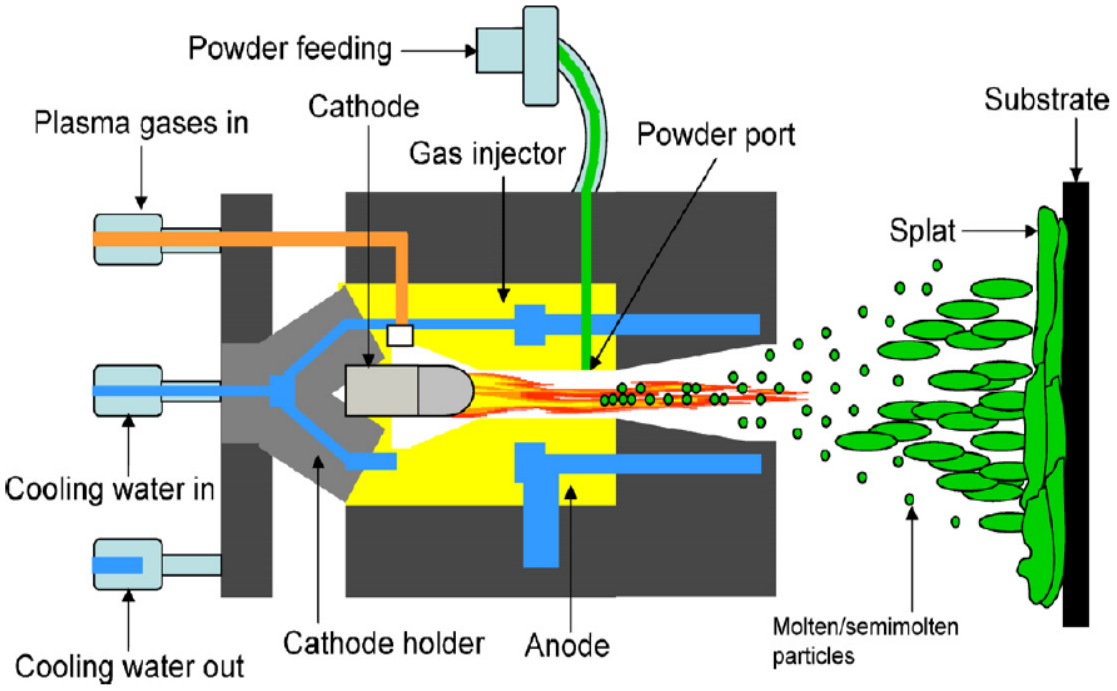

Figure 1.2: Schematic of the plasma spray operation [12]

Mainly, the plasma spraying is carried out in air at atmospheric pressure, namely atmospheric (or air) plasma spraying (APS), and is well adapted to ceramic coating deposition [11],[12]. In this method, the powder is fed along with a high-pressure carrier gas into a heat source of the plasma arc. The plasma plume is produced by passing a primary gas between two electrodes with direct current (DC) or radiofrequency (RF) high voltage discharge. Finally, the inert gas reaches extreme temperatures, dissociates, and ionizes to form a plasma jet [12].

One of the restrictions of the APS process is the minimum thickness of the manufactured coating, which is about $10\mu m$ [13]. The reasons for this limitation are the low flowability of fine particles (i.e., sub-micro meters up to a few micrometers) and difficulties in injecting them into the plasma flow. Therefore, the APS process should be modified to be able to deposit nanophase materials by plasma spraying. In this regard, a liquid medium is used to accelerate small particles and ensure their penetration into the plasma jet. The liquid feedstock is often a suspension of fine particles or a solution [14],[15]. In the former one, called Suspension Plasma Spraying (SPS), a suspension of nano/submicron-sized particles in a base fluid (water or ethanol) is injected into the hot plasma jet [16]. A solution made by dissolving metal powders or liquid metal precursors in a solvent is implemented in the other one. This method is named Solution Precursor Plasma Spraying (SPPS) [14]. In both cases, after evaporation of the liquid medium, the in-flight particles or their agglomerates are treated in the plasma plume. These particles impact the substrate after being heated and accelerated inside the plasma jet and finally generate a coating [15]. Fig.1.3 shows the injection of a suspension into a plasma jet [17].

The possibility of generating improved coating structures by this technique makes it applicable in producing the thermal barrier coating (TBC) for gas turbines and engines, cathode layers in fuel cells (SOFC), biocompatible coatings for implants, silicone-free

solar plants and highly reflective coatings which reduce the thermal load caused by radiation. Therefore, it is expected that a wide variety of research and development is needed to better understand this complex phenomenon [13].

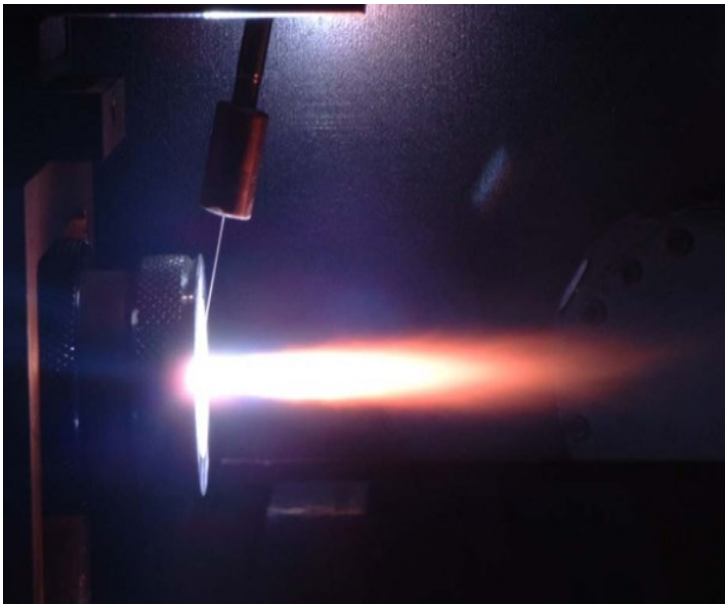

Figure 1.3: Mechanical injection of a suspension into an Ar-H_2 plasma jet [17].

1.3 Liquid Jet Atomization in Suspension Plasma Spray

Considering the suspension plasma spray (SPS) process, breakup and atomization of liquid jets in transverse plasma crossflow are key phenomena that control particles in-flight behavior and coating quality. Fig.1.4 shows a continuous water jet interacted with an air crossflow and a plasma flow [18]. The large ligaments that are very close to the interaction point of the liquid jet and crossflow can be seen in this figure. Afterward, these large ligaments break up into much smaller droplets and control spray trajectories, droplets' size and evaporation. As it is shown, the fragmentations in the two images (highlighted by the arrows) are quite similar. Hence, the hydrodynamic effects are the dominant factor and the thermal effects can be negligible during the rapid primary and secondary breakup mechanisms [9],[18]. Moreover, it is well

demonstrated that instability waves developed along the liquid jet are the roots of the threads, which rapidly broke into big droplets [15].

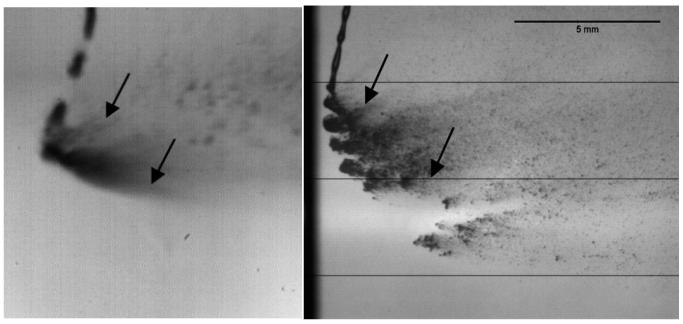

Figure 1.4: Shadowgraph images of water jet interacting with left) an air crossflow right) a plasma flow [18].

As stated above, the suspension plasma spray process is complex and includes diverse parameters affecting the breakup mechanism and the resulting droplet distributions [9],[19],[20]. In this regard, a sufficient jet speed, the optimum diameter of injected droplets, liquid force optimization against that of the plasma, and the effect of other injection parameters have been studied[18],[21]. Furthermore, the effect of different parameters such as substrate and its shape [22], droplet shape and solid concentration [23], arc fluctuations [24], injector angle [25], stand-off distance [16], and liquid column perturbations [9] on the particle movements have been investigated. Concerning LJIC characteristics and mechanisms, liquid jet primary breakup regimes [26]–[30], trajectory and jet penetration [6],[31],[32], droplet features and formation mechanisms [2],[26],[28],[33]–[35] have been explained among numerous researches.

1.4 Previous Studies of LJIC in SPS

Reasonable control of coating deposition in the suspension plasma spray process would be achieved by comprehension mechanisms governing LJIC process and behavior of the droplets in the plasma jet [14]. For instance, the procedures directing thermal and chemical treatments are dependent on the droplet trajectories [36]. On the other hand,

LJIC parameters such as liquid fractions and velocities are challenging to measure locally due to the limitations associated with the current measurement techniques and particular process characteristics. An alternative solution can be the modeling and numerical simulation of the liquid jet interacting with a plasma flow. Detailed numerical simulations will allow us to understand better the breakup mechanism and its effect on the far-field droplets/particles in the harsh plasma spraying process [37]. In continuation, a brief review of the previous studies on modeling the interaction between the liquid jet and plasma flow is reported.

Early numerical works go back to more than a decade ago, where Marchand et al. [14] were the first in coupling a Large Eddy Simulation (LES) turbulence model by Lagrangian modeling of the droplets. They used a three-dimensional (3D) time-dependent model of the plasma jet to study the injection of droplets in a plasma jet, applying it to compute the most significant flow structures. Their study considers the effect of arc fluctuation frequency and amplitude without taking droplet break-up into account. Subsequently, Marchand et al. [38] investigated the effect of mentioned parameters on a single droplet injection. They could categorize the secondary breakup of the droplets according to the gas Weber number (We_g).

In more advanced studies, the penetration of the liquid jet in the plasma and their interaction in terms of liquid interface deformation have been tackled by Vincent et al. [37] and Caryuer et al. [39]. The investigations were based on LES turbulent modeling and the Volume of Fluid (VOF) approach [40], leading to the proposal of a compressible Eulerian model. They increased the droplet inject frequency to infinity to make a continuous liquid jet. A snapshot of the obtained numerical solution is presented in Fig.1.5. Finally, it has been concluded that a more refined computational grid is required in the interaction zone [37]. Above all, the shape of the liquid jet after the interaction was different from the experiments were done by Stenzler et al. [6]. In other

words, they could not find any waves at the liquid-gas interface before the interaction with plasma. Also, Caryuer et al. [39] expressed that their study is not complete because the fragmentation of the liquid is not analyzed.

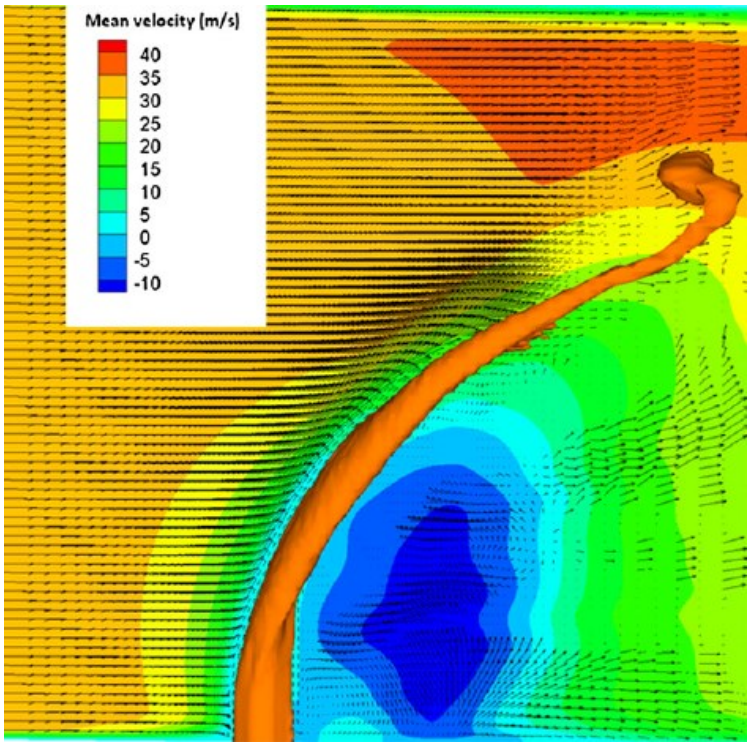

Figure 1.5: A 3D view of the Eulerian VOF acetone jet and the mean velocity in a slice perpendicular to the jet [37].

The simulation presented by Meillot et al. [41] addressed the hydrodynamic interactions between plasma and liquid jets or particles for suspension plasma spraying by modeling the time-dependent behavior of the plasma jet. The FLUENT CFD code, using the RANS turbulence model, was applied to study the injection of Zirconia particles (as Lagrangian particles) in a plasma flow. Later, the plasma and liquid jet interaction was simulated with AQUILON CFD, where the turbulence model was of the LES type. Finally, the liquid jet's primary fragmentation into large drops has been shown (See Fig.1.6). Meillot et al. [41] did not present any quantitative study related to important

atomization parameters such as mean droplet diameter and announced it as their next goal.

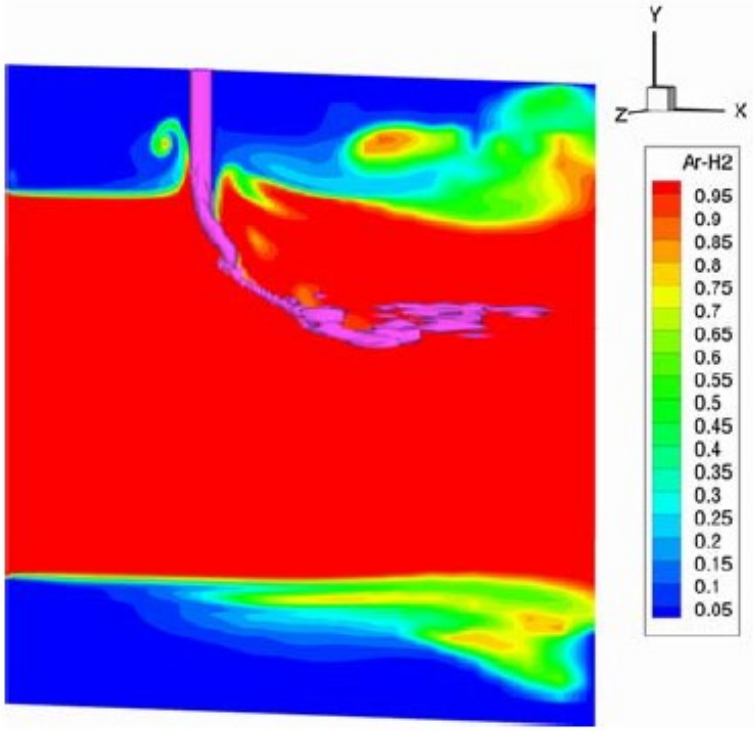

Figure 1.6: Vertical cross-section of a plasma and liquid jet concentration [41]

In a more recent study, Meillot et al. [15],[42] investigated the interactions between a continuous jet of pure water and a plasma jet using only Navier-Stokes and heat equations. An Eulerian approach has been performed to solve the fluid mechanic equations and a 1-fluid model is used to consider the compressible effects. The interface of the two phases has been tracked by the VOF method. The interactions at different times of liquid jet penetration into plasma flow have been figured. Moreover, instability waves developed along the liquid column have been found [15],[42].

Shan et al. [43] numerically investigated liquid stream and gas-blast injection modes concerning the droplet size distribution. A three-dimensional (3D) and time-dependent model with the RNG-based k_ε model was carried out. Eventually, the particle/droplet

size and position distributions were predicted. It has been concluded that, in the liquid jet mode, the solution droplets penetrate more into the plasma jet compared with the gas-blast injection mode.

Using an Eulerian method and modeling injected droplets using a Lagrangian approach, the results such as the droplet/particle trajectory, velocity, and temperature of suspension feedstock in plasma spraying, have been obtained. In this type of simulation, a suspension jet is injected in the form of droplets. For instance, Jabbari et al. [19] used a three-dimensional two-way coupled Eulerian-Lagrangian approach while the plasma jet fluctuations were neglected. The authors implemented Reynolds Stress Model for turbulence modeling. For the secondary breakup, KHRT (Kelvin-Helmholtz Rayleigh-Taylor) model is utilized. The particle behavior near the substrate, the effect of substrate and droplet shape, solid concentration, and arc parameters on droplet characteristics [16], [22]–[24],[44] have been investigated using similar numerical models. Furthermore, Farokhpanah et al. [45] applied similar approaches and $k-\epsilon$ turbulence model to explore the effects of injector parameters. Xiong et al. [46] illustrated the atomization of the droplets using cascade atomization and droplet breakup (CAB) model. They showed that the fragmentation of liquid stock mainly controls the spraying details.

1.5 Present Study and Objectives

From the previous sections, it can be concluded that the atomization of a liquid column in a crossflow is an important phenomenon in suspension thermal sprays and should be fully understood. Detailed qualitative observations along with quantitative data of the interactions between the liquid jet and plasma flow are required to predict the droplet size distribution and consequently control the coating buildup. Compared to the numerical simulations, the experimental observations in plasma and wind tunnel

conditions can not provide results in detail. In addition, the previous numerical simulations of the SPS process could not provide breakup characteristics of the liquid jet thoroughly. Specifically speaking, a detailed picturing of the jet breakup mechanism in plasma spraying is missing, and recent studies suffer from the lack of knowledge about the effect of hydrodynamic forces on breakup regimes and droplets characteristics. Therefore, in the field of suspension plasma spraying, supplementary studies should be conducted to obtain more information about suspension-solution breakup model and particles behavior in the far-field. This statement determines the primary motivation of the present work. The objectives of this work which is predominantly a numerical study, can be summarized as follows.

- Explore the effect of density ratio(r_ρ), gas Reynolds (Re_g) and gas Weber (We_g) numbers on the liquid jet breakup process.
- Investigate liquid jet penetration and transition from primary to secondary atomization in a plasma cross flow.

In addition, the contents of the next chapters are briefly explained as follows.

Chapter 2- Methodology

In chapter 2, numerical methods that have been implemented by the software program are described. The solver is called Basilisk and has been found perfectly efficient in simulating the atomization process while utilizing the benefits of an adaptive mesh refinement method. Moreover, the simulation setup and the flow parameters of each case study along with non-dimensional numbers, have been explained in detail. Indeed, chapter 2 demonstrates the utilized assumptions in performing the numerical simulation of breakup phenomena of a liquid jet in the plasma flow. In the second

chapter, a case study holding wind tunnel parameters has been investigated to compare the results of plasma crossflow with air one.

Chapter 3- Results and discussions

The task of presentation and interpretation of the obtained results has been done in this chapter. Qualitative and quantitative comparisons of near-field breakup properties of considered cases have been explained in this chapter. For instance, jet trajectory, breakup location, and instability waves generated along the jet column have been discussed. Furthermore, droplet size distribution is the other object that has been covered to complete this section of the thesis.

Chapter 4- Conclusion and future works

This chapter includes a summary and conclusion of the present investigation. Finally, some recommendations are presented for future research.

Chapter 2

Methodology and Modeling Technique

2.1 Introduction

Today, the two-phase flow field draws significant attention in primary and applied sciences. For instance, the two-phase flow phenomenon is encountered in the drop impact involved in ink-jet printing, combustion chambers, liquid jet atomization, pesticide sprays, and raindrop splashing on the ground. Also, this field is applied in geophysical contexts like river motion, ocean dynamics, and large-scale water waves [47]. In particular, two-phase flow is prevalent in the atomization process in thermal sprays and combustion chambers [48],[49]. In this type of flow, the interface separates two domains with different flow properties and is a challenging dynamic problem. Fortunately, the recent progress in high-speed imaging has substantially improved the comprehension of two-phase flows. Currently, addressing the problems that were unachievable a few years ago is possible by using experimental developments and

numerical methods improvements. Therefore, the interest in simulating more complicated and realistic two-phase flow has risen remarkably [48].

This chapter is organized as follows. Firstly, the equations governing the dynamics of a liquid jet interacting with a crossflow are introduced. Then the implemented numerical scheme is presented. The utilized method combines volume-of-fluid (VOF) that tracks the interface and adaptive mesh refinement (AMR), which optimizes the numerical calculations. Additionally, the implemented solver has been illustrated as well as the grid adaptation method. In the end, the simulation setup of the different simulated cases is specified.

2.2 Governing Equations

A review of the governing equations implemented in this study for simulation of liquid jet atomization in a crossflow is provided here. It should be noted that in a conventional atmospheric plasma spray, the Mach number is typically less than 0.5 since the gas temperature is high. In time-dependent problems, the maximum value of the timestep can be under restriction due to the finite speed of sound waves in low Mach number flows. A helpful approach to remove this limitation is considering the fluid incompressible [50]. Therefore, the mixture of immiscible liquid and gas is assumed to be incompressible at low Mach numbers. Finally, a single fluid formulation demonstrates the two-phase flow of liquid and gas, and the incompressible variable-density form of Navier-Stokes equations with surface tension can be written as follows:

$$\nabla . \boldsymbol{u} = 0, \tag{1}$$

$$\rho \frac{\partial \boldsymbol{u}}{\partial t} + \rho \boldsymbol{u} . \nabla \boldsymbol{u} = -\nabla p + \boldsymbol{f} + \mu \nabla^2 \boldsymbol{u} + \sigma \kappa \delta s \boldsymbol{n}, \tag{2}$$

Where ρ is density, $\boldsymbol{u}$ is the flow velocity field, μ is the viscosity, p is the pressure, and $\boldsymbol{f}$ is the body force vector. The surface tension force is represented by a singular term (the fourth term on the right-hand side of Eq.2), where a Dirac distribution function δs localized on the interface. In the second equation, σ is the surface tension coefficient, κ is the local curvature, and $\boldsymbol{n}$ is the normal unit vector of the interface. In this study, the surface tension coefficient σ is considered constant. The two different phases are recognized by a characteristic color function called C. Actually, this function presents the position of each phase and can be obtained by solving the following advection equation, which is satisfied by the temporal evolution of each phase.

$$\frac{\partial C}{\partial t} + \boldsymbol{u}.\nabla C = 0, \tag{3}$$

2.3 Numerical Method

Most practical multiphase flow problems reveal high surface tension, high liquid-to-gas density ratios, complex interface, and spatial scales with different orders of magnitude. These are the characteristics that are involved in the simulation of a liquid jet interacting with plasma spray crossflow. In this framework, an ideal scheme for the solution of the above equations should be capable of efficiently representing the evolving interfaces, curvature, and flow features with different spatial scales [48]. Literally, all these goals are the main features of the utilized numerical method. They should be reached robustly in a high-density ratio domain such as SPS, where a Liquid Jet in Crossflow (LJIC) problem is encountered.

Here, the essential steps that are related to resolving the interfacial two-phase incompressible flows are summarized. To tackle the problem, the momentum-conserving volume-of-fluid (MCVOF) is employed [51]. In the VOF method, the

advection equation (Eq.3), is solved in its integral form. To find viscosity and density values, the following equations have been used where subscribes "g" and "l" represent gas and liquid phases in respect. The local value is calculated based on VOF approach (variables without a subscript), where f is the mean value of C in the cell. The f value can be 1, 0 or a fractional number between them, to present reference phase (fluid), the second phase (gas), and the interface cell, respectively.

$$\rho = f\rho_l + (1-f)\rho_g, \tag{4}$$

$$\mu = f\mu_l + (1-f)\mu_g, \tag{5}$$

The volume-fraction flux $F_{f,i}$ in the direction of i is demonstrated as below [52].

$$F_{f,i} = f_a u_{f,i} S, \tag{6}$$

Where S is the surface area, $u_{f,i}$ is the component of the velocity at the cell surface and f_a is the fraction of the fluid advected the cell surface. In Eq.6, f_a, is obtained based on the reconstruction of the interface and implementing the piecewise linear interface construction (PLIC) technique [53]. Indeed, the VOF method using the PLIC technique is applied to track the gas-liquid interface and estimate the material properties at the interface. The Mixed-Youngs-Centered (MYC) [54] is used to compute the interface normal, and the location of the interface in a cell is calculated based on the method of Scardovelli and Zaleski [55].

Regarding the momentum advection, Eq.2, the primary requirement is the consistency of this equation with the advection of volume fraction in Eq.3 [52]. The finite-volume approach is used to discretize the momentum equation. Afterward, to discretize the surface tension term and obtain the interface's local curvature, a balanced forced

approach [56] and height-function method [57] are utilized, respectively. Likewise, a classical projection method is used, leading to a linear equations system for unknown pressures. The corrected velocity is obtained using the solution of the pressure Poisson equation. Furthermore, a classical multigrid "V-cycle" is applied to accelerate the solution of the system of equations [58]. The Bell-Collela-Glaz (BCG) [59] second-order upwind scheme is performed to reconstruct advected liquid and gas momentum per unit volume.

2.4 Numerical Solver and Spatial Discretization

The built-in solvers that have been implemented in the numerical method mentioned above are applied in the open-source code, Basilisk (http://basilisk.fr). Basilisk software provides the solution of partial differential equations on an adaptive mesh that will be discussed later. This software is the inheritor of the Gerris software and was developed by the same developers [60]. This code performs a second-order accurate finite-volume approach based on a projection method for Navier-Stokes equations. In other words, the consistency of the momentum flux with volume-fraction flux is undemanding by collocating mass and momentum control volumes in a spatial discretization manner. Also, the second-order accurate time discretization is obtained from a staggered-in-time discretization of volume-fraction/density and pressure [52]. In Basilisk, the MCVOF advection of velocity components for a two-phase Navier-Stokes solver is conducted in "conserving.h" which implements the VOF advection tracer method ("vof.h").

As discussed above, one of the characteristics of two-phase flows in LJIC problems is the wide range of the encountered spatial scales. Consequently, a few researchers have investigated an adaptive spatial discretization that accompanies the spatiotemporal evolution of flow structures [50],[61]–[63]. The hierarchically structured grid approach [63] (adaptive mesh refinement, AMR) and quad/octree-based (2D/3D) discretization

[61],[64] have been developed for compressible flows. For the incompressible one, the AMR has been implemented by [62],[65],[66]. Furthermore, a multigrid solver is well ordered for elliptic or parabolic problems. One can show that these solvers require only $O(N)$ operations to solve a Poisson-Helmholtz equation discretized with N grid points [67],[68]. The hierarchical approach is applicable for multigrid solver and, flexibility and clarity of quad/octree discretization is a notable advantage in dealing with evolving interfacial flows. It has been demonstrated that geometric multigrid can be merged with quad/octree spatial discretization and prepares an adaptive algorithm for expensive problems such as incompressible Navier-Stokes flows [50],[68]. The adaptive mesh refinement has been implemented within the Basilisk framework. This software performs a direct numerical simulation by combining an adaptive quad/octree spatial discretization, geometrical Volume-Of-Fluid interface representation, balanced-force continuum-surface-force surface-tension formulation and height-function curvature estimation [57],[69]. The reader is invited to seek the Basilisk website and references therein for more documented information and description of the source codes.

About spatial discretization, the domain is refined using square finite volumes ordered hierarchically as a quadtree (octree in 3D). An example of the quadtree mesh technique is represented in Fig.2.1, where each finite volume is referred to as a *cell*. The numbers in the figure show the level of the cells in the tree that is an essential parameter. The logical (tree) can be considered as a "family tree" where the *root* cell is the base of the tree (has level zero), and a *leaf* cell is a cell without any *child*. The level increases by one after each consecutive generation and adding a group of four descendant children. Indeed, each *parent* cell can have up to four *children* in the 2D domain and eight in 3D. To simplify the problem, the level of the adjacent cells cannot differ by more than one. This rule leads to 1) neighboring cells being on the same level. 2) two fine cells are neighboring the same coarse cell. In this regard, the red and blue ghost points act as

virtual cells that provide all cells with neighbors with the same refinement level, see Fig.2.1.b. The red and blue dots represent the down-sampling and up-sampling operations, respectively. This tree allows an efficient adaptive mesh refinement to perform multiresolution analysis of a field [50],[70],[71].

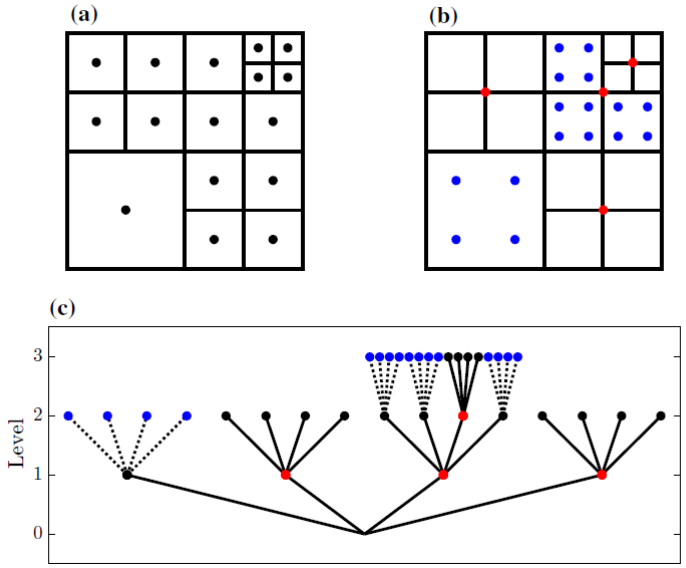

Figure 2.1: Example of a tree-grid structure. a) spatial structure of the grid cells. b) location of two types of ghost points. c) corresponding tree representation at different levels [70].

It should be mentioned that a domain decomposition algorithm is carried out to provide Basilisk software capable of parallel running on many processors using Message Passing Interface (MPI). As the grid is locally refined or coarsened, the domain decomposition between processors must be updated to balance the load. The solver can perform this task using a natural decomposition applied to the quad/octree mesh technique [70],[72]. Coupled with adaptive grids, the solver allows efficient and very high-resolution modeling on large parallel systems [68]. In more recent research, a detailed numerical simulation is performed to study the primary breakup of a gasoline fuel injection and atomization [52]. Furthermore, Popinet [68] has implemented the

solver to model the Tohoku tsunami of March 2011 in Japan, which includes large spatiotemporal scales.

2.5 Operating Conditions

As stated in the previous chapter, a LJIC phenomenon is involved in the SPS process and leads to the liquid jet breakup and producing large ligaments and small droplets. Fig.2.2 shows a schematic of this phenomenon. As the plasma temperature is about 13000 K at the plasma torch exit plane [73], its density is very low compared to the injected liquid jet. Therefore, the process is an extremely complex LJIC problem due to reasons such as liquid column instabilities due to high-density ratio ($r_\rho = \rho_l/\rho_g$). Normally, the behavior of the LJIC is described with these non-dimensional parameters: viscosity ratio $r_\mu = \mu_l/\mu_g$, density ratio $r_\rho = \rho_l/\rho_g$, gaseous Weber number $We_g = \rho_g u_g^2 d_o/\sigma$, momentum flux ratio $q = \rho_l u_l^2/\rho_g u_g^2$ and crossflow Reynolds number $Re_g = \rho_g u_g d_0/\mu_g$. Where d_o and σ are diameter of liquid nozzle exit and liquid surface tension, respectively. The fundamental investigation of the effect of each parameter is required to control the SPS process and comprehend the breakup physics. The following parts present the numerical parameters used to simulate the breakup mechanism.

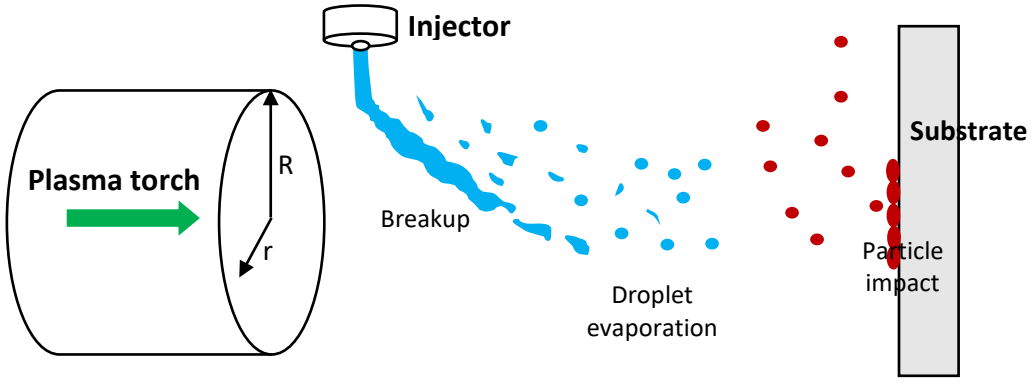

Figure 2.2: Phenomena involved in plasma spraying of solution precursors and suspensions

Physical Parameters

Considering an argon plasma crossflow, the velocity and temperature fluctuations can be negligible, and the profiles are functions of the space only. To perform the simulations, the velocity (u_g) and temperature (T_g) profile at the torch exit of an argon plasma flow were obtained from the work of Wan et al. [73].

$$u_g = u_m \left(1 - \left(\frac{r}{R}\right)^{1.2}\right) \tag{7}$$

$$T_g = T_a + (T_m - T_a)\left(1 - \left(\frac{r}{R}\right)^{6}\right) \tag{8}$$

Where r is the radial distance and R is the exit radius of the plasma torch and equals 3.75 mm here (see Fig. 2.4.). $T_a = 300$ is the ambient temperature and u_m and T_m which are velocity and temperature at the centerline and are considered $1700\, m/s$ and $12{,}300\, K$, respectively [73]. Also, density (ρ_g) and viscosity (μ_g) of argon plasma gas can be considered functions of plasma temperature. Finally, we have u_g , ρ_g and μ_g and consecutively We_g and Re_g that all are functions of r, and their mean value over the region $\mathbb{R}$ can be calculated using:

$$\bar{F} = \frac{1}{A} \iint_{\mathbb{R}} F(r).dA \tag{9}$$

Here, the region $\mathbb{R}$ is the plasma torch exit which is circular with radius R=3.75 mm, $A = \pi R^2$ and $dA = rd\theta.dr$. Applying Eq.9 for We_g and Re_g leads to obtaining mean values of these parameters at the torch exit. For example, the mean value of $We_g(r)$ can be calculated as follow, using Eq.7:

$$\overline{We}_g = \frac{1}{\pi R^2} \int_0^R \frac{\rho_g(r).u_g^2(r).d_o}{\sigma} 2\pi r.dr \quad (10)$$

Regarding the suspension plasma spray process, the suspension can be prepared by dispersing the powder in water or ethanol [13]. Considering $d_0 = 250\ (\mu m)$, $\sigma_{water} = 0.0708\ (\frac{N}{m})$ and $\sigma_{ethanol} = 0.022\ (\frac{N}{m})$ the following results are obtained: $\overline{We}_{g,water} = 78$ and $\overline{We}_{g,ethanol} = 250$. Where d_0 is the diameter of the injection orifice. Implementing the same approach and Eq.9, $\overline{Re}_g = 32$, $\bar{\rho}_g = 0.078\ (\frac{kg}{m^3})$ and $\bar{\mu}_g = 0.00047\ (\frac{kg}{m.s})$ would be acquired. Consequently, concerning $\rho_{water} = 997\ (\frac{kg}{m^3})$, $\rho_{ethanol} = 790\ (\frac{kg}{m^3})$, $\mu_{l,water} = 0.000894\ \left(\frac{kg}{m.s}\right)$ and $\mu_{l,ethanol} = 0.001095\ \left(\frac{kg}{m.s}\right)$, and averaging the liquid to gas density ratio and viscosity ratio for these two liquids, we will have $r_{\rho,average} = 11750$ and $r_{\mu,average} = 4.22$.

When it comes to liquid jet velocity and momentum flux ratio (q), the mass flow rate of the liquid was taken 20, 30, and 40 $\left(\frac{g}{min}\right)$. Respecting $\dot{m} = \rho_l u_l (\frac{\pi}{4}) d_o^2$, u_l value of water and ethanol liquids can be calculated for mentioned mass flow rates. Substituting u_l values in $We_l = \rho_l u_l^2 d_o/\sigma$ and using mentioned values of density and surface tension for water and ethanol, six liquid Weber numbers can be achieved. According to the definitions of the dimensionless numbers, $q = \frac{We_l}{We_g}$. The mean value of We_g has been calculated previously for water and ethanol. Thus, momentum flux ratios for water and ethanol cases and different mass flow rates are obtained. The results show that $2 < q < 11$. With reference to $\mu_{l,water}$ and $\mu_{l,ethanol}$, Re_l can be obtained for different mass flow rates. It has been demonstrated that the liquid Re number is between 1550 and 3810. Finally, the primary parameters governing suspension-solution plasma spray processes have been obtained. The obtained values are presented in Table 2.1 and demonstrating the two case studies of the thesis.

Table 2.1: Primary parameters controlling suspension plasma spray processes

r_ρ	r_μ	$We_{g,water}$	$We_{g,ethanol}$	q	Re_g	Re_l
11750	*4.22*	*78*	*250*	*10*	*32*	*2600*

Similar results for $\overline{Re_g}$ and $\overline{r_\rho}$ were obtained in [74]. It should be noted that for a liquid jet in a crossflow under the atmospheric conditions in a wind tunnel, the values of Re_g and r_ρ are completely different with Table 2.1. (i.e. Re_g is about two orders of magnitude higher and r_ρ is one order lower) [75]. In this regard, we increased the Re_g to 3200 and decreased the r_ρ to 1175 to have a new case representing the conditions in a wind tunnel. Finally, three cases in total have been arranged and investigated in this study. Tables 2.2 and 2.3 reveal a summary of the thermo-fluid conditions of these cases. In these simulations U_g= 54.8 m/s, ρ_g = 1.18 kg/m^3, and $d_0 = 8 \times 10^{-4}$ m. As it introduced in chapter 1, the Ohnesorge number can be obtained by using $Oh=\mu_l/\sqrt{\rho_l \sigma d_0} = \frac{We_l^{0.5}}{Re_l}$. It is worth mentioning that the values of density, viscosity, surface tension, velocity, etc., were changed in such a way that the calculated non-dimensional numbers were not altered.

Table 2.2: Primary dimensionless numbers ($Re_l = 2600$)

Case	*Crossflow*	r_ρ	r_μ	We_g	q	Re_g	Oh
A	*Air*	*1175*	*133*	*78*	*10*	*3200*	*0.01*
P1	*Plasma*	*11750*	*4.22*	*78*	*10*	*32*	*0.01*
P2	*Plasma*	*11750*	*4.22*	*250*	*10*	*32*	*0.02*

Table 2.3: Fluid and flow properties (U_g= 54.8 m/s, ρ_g = 1.18 kg/m^3, and $d_0 = 8 \times 10^{-4}$ m)

Case	*Crossflow*	$\rho_l(kg/m^3)$	$\mu_l(kg/m.s)$	$\mu_g(kg/m.s)$	$\sigma(N/m)$	$U_l(m/s)$
A	*Air*	*1386.5*	*0.00216*	*0.00001617*	*0.036*	*5.06*
P1	*Plasma*	*13865*	*0.006826*	*0.001617*	*0.036*	*1.6*
P2	*Plasma*	*13865*	*0.006826*	*0.001617*	*0.0113*	*1.6*

In this study, the focus is understanding the effect of r_ρ and We_g. The simulations are performed in a rectangular computational domain with dimensions of 4.7×4.7×4.7 cm^3. This large computational domain (which is approximately 59*d_0) is chosen to capture the details of spray behavior in near-field and far-field. Fig.2.3 demonstrates a schematic of the computational domain. As it was shown, the x and y axes are in the directions of crossflow and liquid jet injection, respectively. The center of the circular liquid jet orifice is located at (0.0, 0.0, 0.0), and the orifice diameter is $0.8mm$. A Dirichlet boundary condition and the uniform velocity profile (U_g) are imposed at $x = -7.8mm$ plane to simulate crossflow inlet. Furthermore, the no-slip boundary condition is applied at the $y = 0$ plane, except at the jet orifice where Dirichlet boundary condition and uniform velocity profile (U_l) are imposed for jet inlet velocity. For the rest of the boundary planes, the outflow boundary is implemented (See Fig.2.3.). Also, the inlet velocity of crossflow (air or plasma) and liquid jet can be found in Table 2.3. An adaptive mesh refinement with 11 levels of refinement is implemented to refine the grids near the liquid-gas interface and model the small scales turbulent flow accurately in both phases. Therefore, regarding domain dimensions, the finest grid size reaches $\Delta x = 22.9\ \mu m$.

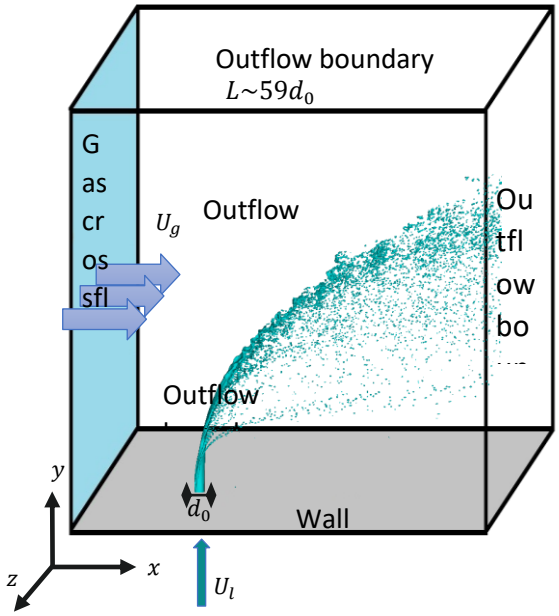

Figure 2.3: Schematic view of the cubic computational domain.

As it demonstrated in previous sections, a fundamental and parametric study of the breakup physics of liquid jet in plasma crossflow is a key in controlling suspension plasma spray prosses. In the present study, numerical simulations are performed to show what breakup characteristics will (or will not) alter if we switch Re_g and r_ρ of a wind tunnel (air crossflow) to a harsh condition such as argon plasma. Specifically, breakup characteristics such as spray plume boundaries, jet column instability waves, breakup point, and jet column shape are investigated in the next chapter. Moreover, the effect of plasma crossflow properties on the size of the far-field droplets has illustrated in the next chapter.

Chapter 3

Results and Discussion

The breakup of a liquid jet in crossflow (LJIC) is of great importance to SPS process where suspension liquid jet interacts with a plasma crossflow. It has been illustrated previously that controlling the obtained coating quality can not be achieved without studying the breakup mechanism of the liquid jet. In this chapter, the qualitative and quantitative data post-processed from the simulations are presented to better understand the effect of dimensionless parameters like r_ρ and Re_g . Three case studies have been introduced in the preceding chapter. In case "A" which represents an experience in the wind tunnel, airflow is considered as a crossflow. In the other two cases ("P1" and "P2"), plasma is taken part as gas crossflow. In the last two cases, r_ρ and Re_g are respectively one order of magnitude higher and two orders lower than case "A" (See Tables 2.2 and 2.3).

Before demonstrating the result, the methodology and solver are validated against the data available in the literature. In this regard, a comparison of the instantaneous snapshots of the liquid jets and the near-field breakup properties are presented in the following.

3.1 Validation

Li and Soteriou [75] numerically simulated some cases that are configured based on the experiments by Sallam et al. [76]. Indeed, near-field characteristics of a non-turbulent LJIC have been measured at conditions that $r_\rho = 845$, $Re_g = 2781$, $We_g = 40$ and $q = 88$ [75]. Fig. 3.1. compares the snapshots of side-view images. Clearly, the present study not only captures a similar breakup mechanism but also presents more details of the jet column features and droplet formation.

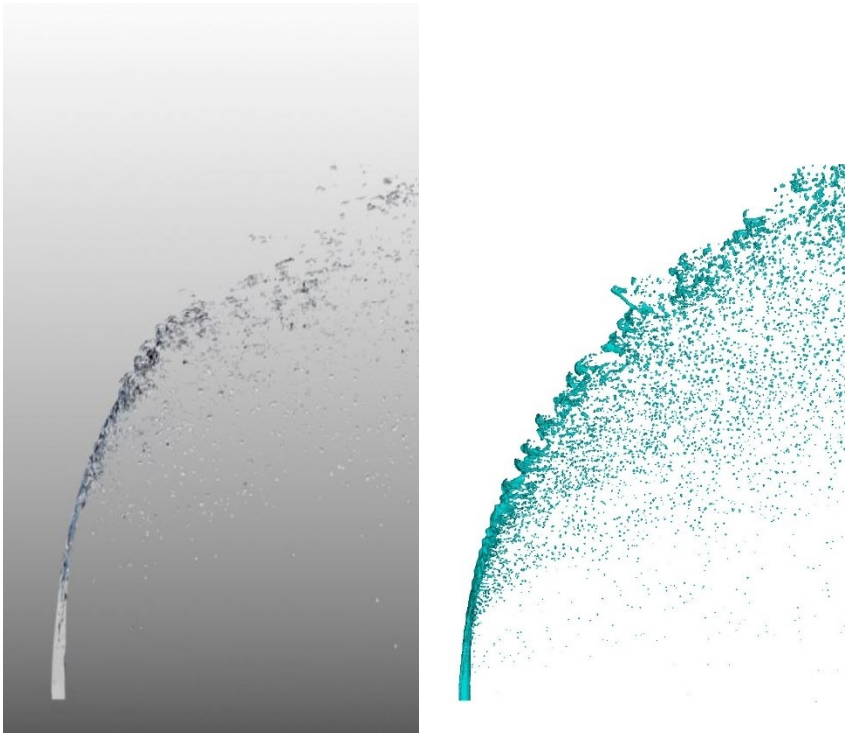

(a) (b)

Figure 3.1: Validation of the instantaneous snapshots of the liquid jet breakup; (a) Li and Soteroiu [75], (b) present study.

An additional comparison of the atomization process is presented in Fig. 3.2, where the shape of the jet at xz plane cross-sections at different heights are figured to better validate our simulation qualitatively. As it is shown, the degree of column flattening and striping are matched in a sensible way.

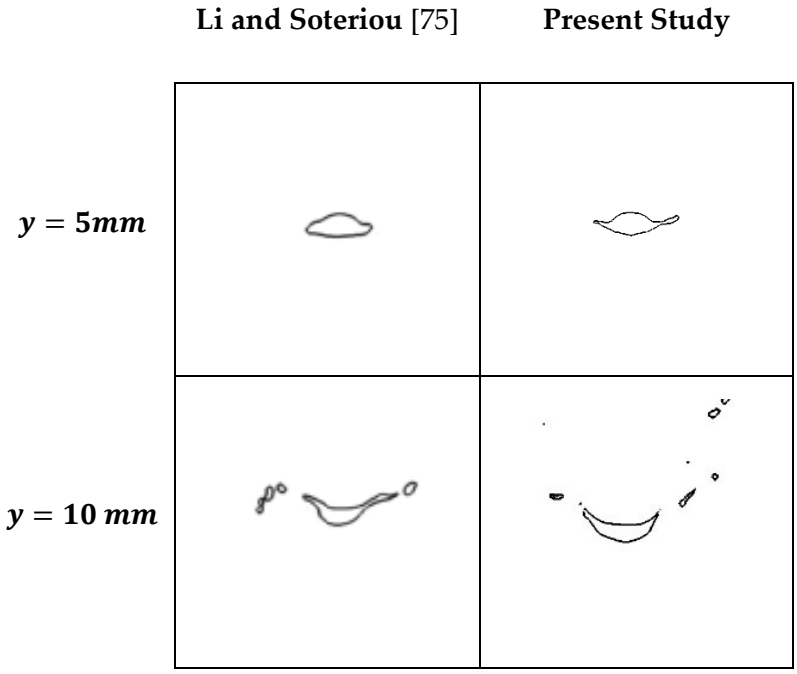

Figure 3.2: Validation of jet column shape in the XZ plane cross-sections.

When it comes to the quantitative data, the location of the breakup point and length of the surface waves responsible for the onset of the column breakup can be considered. It is evident that recognizing surface waves and jet fracture point is problematic from the xy view due to hiding issues (See Fig. 3.1). To tackle the complexity of the liquid shape, the liquid surface has been decomposed into consecutive thin slices in the transverse z direction. Fig.3.3 shows a colormap image of the liquid surface at $z = 0$. Clearly, the surface slicing has eliminated the ligaments and droplets blocking the jet column's view.

The initial surface waves are recognized visually for calculating the wavelength, and the distance between two consecutive picks is obtained. Operationally defined, the length of a wave-containing section has been divided by the number of the waves within that section (See Fig.3.3.).

Regarding the breakup point location, it has been considered where the jet column loses its coherence, and the fragmentation happens. The first ligament pulled off from the jet

column in the breakup area should be found to obtain this point. Then, a point on the jet column with the shortest distance from this ligament is named the breakup point, as shown in Fig.3.3. It should be mentioned that measuring the breakup point and the length of the instability waves are repeated for 50 consecutive snapshots. These snapshots are selected from a $1ms$ time interval in the quasi-steady state. In this state, the number of droplets in the computational domain is almost constant (less than 1% variation).

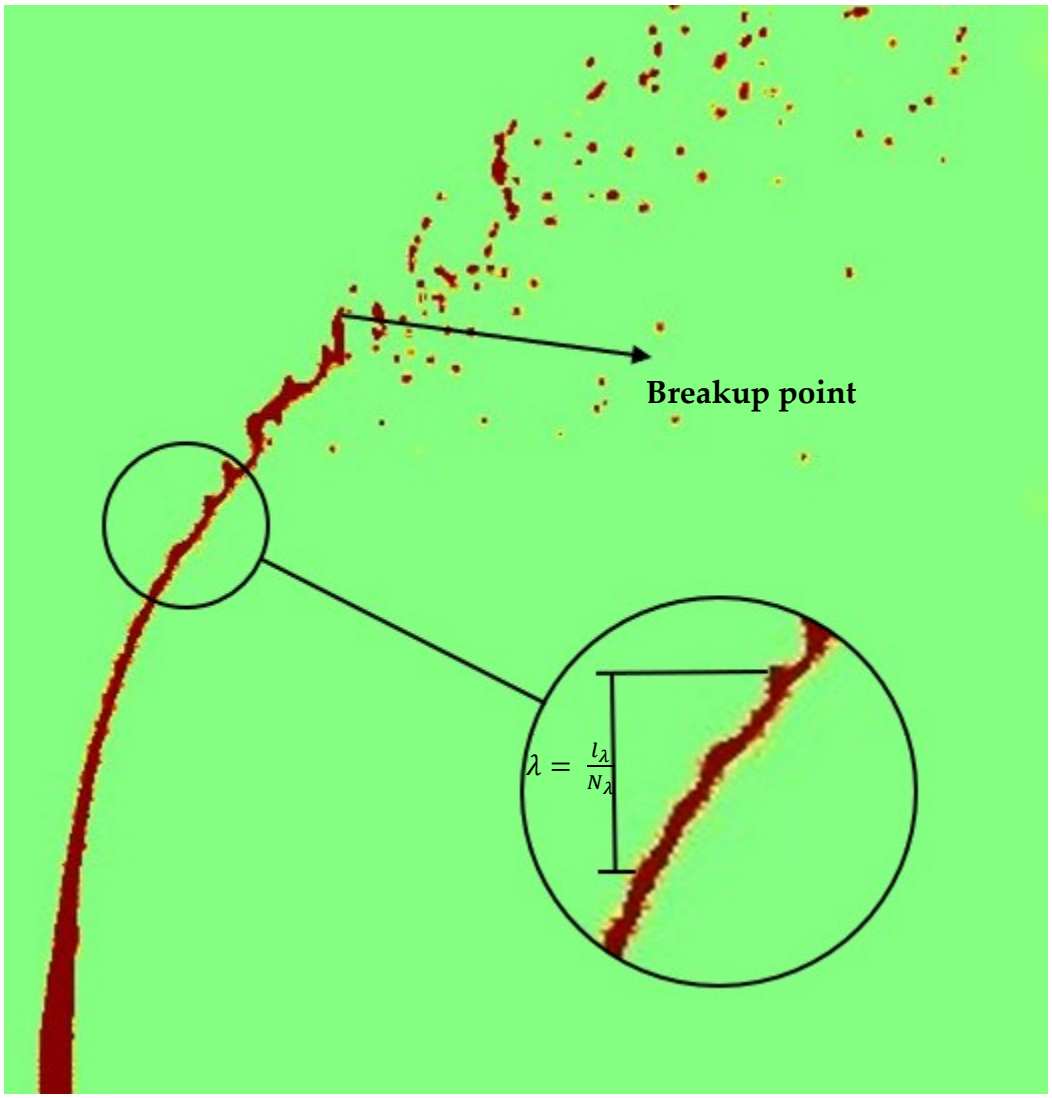

Figure 3.3: Decomposed liquid surface used to quantify the breakup location and wavelength.

Sallam et al. [76] achieved the best-fit correlation of the wavelength measurements as a function of Weber number [76]. This correlation can be expressed for values of $Oh < 0.12$, $3 < q < 8000$ and $We > 4.0$ as follows:

$$\frac{\lambda}{d_0} = 3.4We^{-0.45}. \tag{11}$$

Also, their experimental measurements predicted the locations for the liquid column fracture and are stated in Table 3.1. This table shows that the present study simulations compare reasonably well with Li and Sotreriou's [75] numerical analysis and the experimental correlation of Sallam et al. [76].

Table 3.1: Comparison of the location of breakup point and length of surface waves

Case	$\frac{x_b}{d_0}$	$\frac{y_b}{d_0.q^{0.5}}$	$\frac{\lambda}{d_0}$
Present Study	*8.8*	*2.75*	*0.77*
Li and Soteriou [75]	*~7.8*	*~2.0*	*0.75*
Sallam et al. [76]	*8.0*	*2.5*	*0.65*

3.2 Qualitative Comparison of the Jet Atomization Process

As mentioned before, *Case A*, represents a case considering air as a crossflow and *Case P1* and *Case P2* consider jet atomization in the plasma spray condition. In *Case A*, Re_g is two orders of magnitude higher and r_ρ is one order lower than other two cases ($Re_{g,A} = 3200, r_{\rho,A} = 1175$). Furthermore, the high viscosity of the plasma gas led to a lower viscosity ratio of plasma cases compared to *Case A* (See Tables 2.2 and 2.3). Concerning *Case P1* and *Case P2*, the only difference between them is the gas Weber number

($We_{g,P1} = 78, We_{g,P2} = 250$) and other vital parameters kept constant. It should be mentioned that the instant time of the simulations is when the jet is injected into a crossflow. The atomization process reached the steady-state after $5.5\,ms$, $9.5\,ms$ and $8.5\,ms$ for *Case A, Case P1* and *Case P2,* respectively. The simulations were performed for more than $1\,ms$ after reaching steady-state to have enough data for the post-processing step. Generally, the total cost for each simulation was about twenty days using ~166 processors and ~500 GB memory. A liquid jet penetrated a crossflow has been displayed in Fig 3.4. Implementing adaptive mesh refinement (AMR) led to finer cell size at the liquid-gas interface and where there are velocity fluctuations.

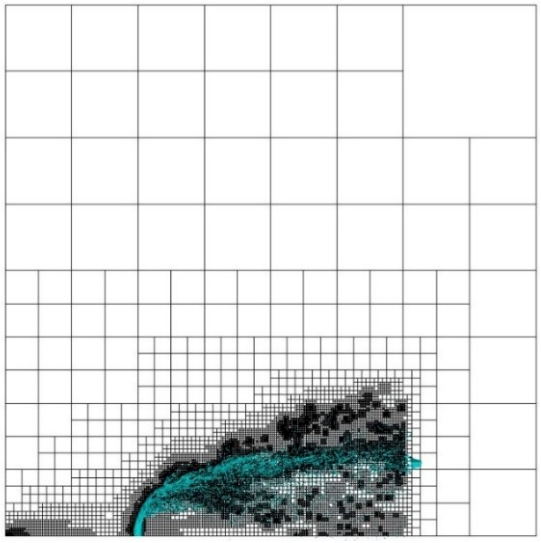

Figure 3.4: Implementing AMR to simulate the interaction of liquid jet and crossflow

The atomization features of liquid jets in crossflows for the three cases are qualitatively compared using liquid surface images in three orthogonal views. The snapshots of liquid jet breakup in xy plane (side-view), yz plane (windward view) and xz plane at the same time are demonstrated in Fig 3.5. It is observed that as the jet penetrates into the crossflow, it bends towards the crossflow stream. The jet bending degree of the jets injected in the plasma crossflow looks a little higher than air crossflow (See Fig 3.5 (a-c)).

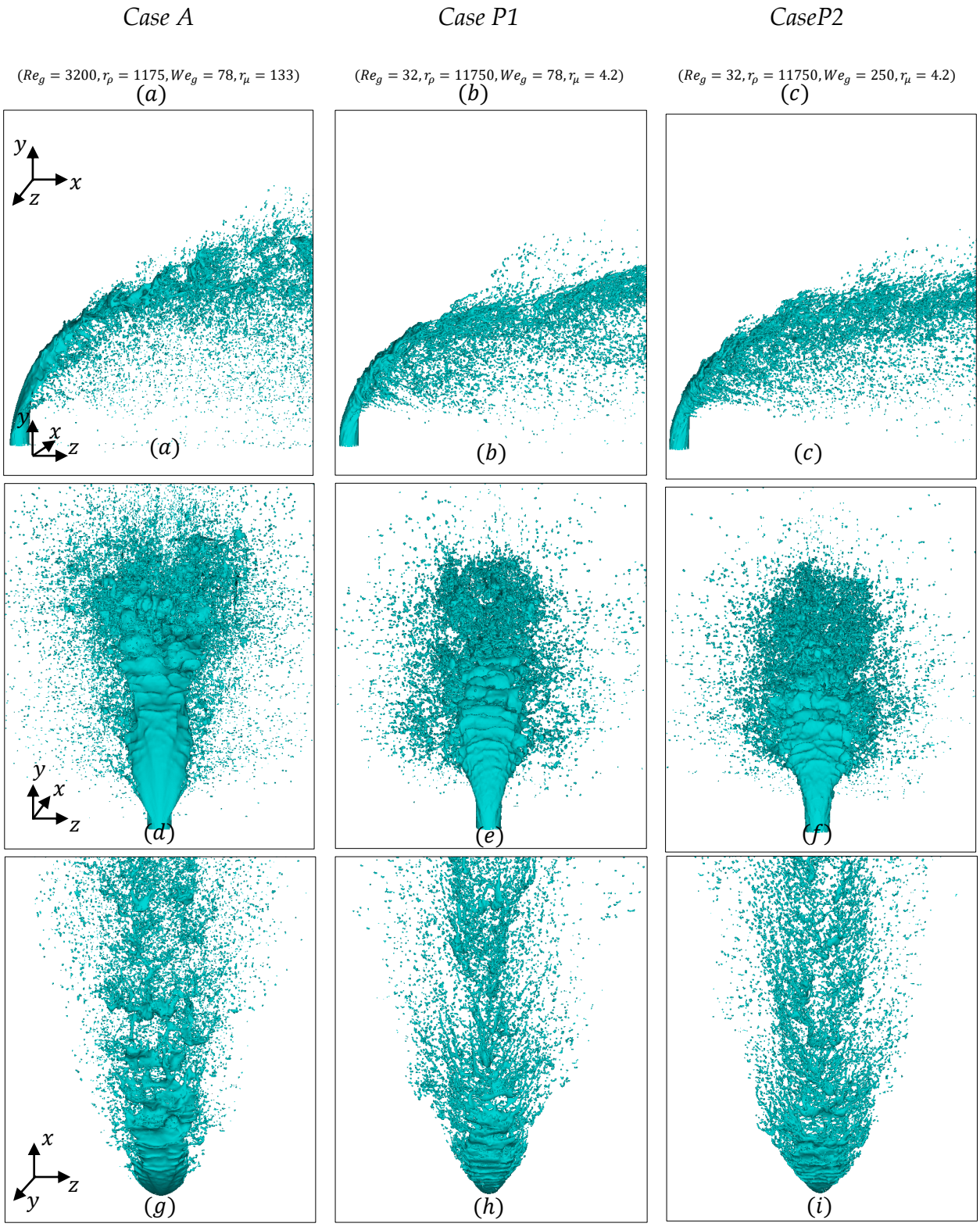

Figure 3.5: Instantaneous snapshots of liquid jet breakup in crossflow in different views

As can be seen, instability waves are formed on the column windward surface and cause the ligaments and small droplets to disintegrate. Also, surface stripping on the edge of the flattened column is promoted by the instability waves. This surface stripping mechanism depletes the jet column before reaching the column breakup point. The point is that the produced droplets of this mechanism do not have enough inertia and consequently penetrate less in the jet injection direction (positive y direction).

Song et al. [77] and Li et al. [78] concluded that the most dominant parameter in jet penetration height is the momentum flux ratio, q. This fact can be confirmed in this study too, as q is fixed among all the three cases and the jet penetration height has not changed significantly (See Figs 3.5 (a-c)). Nevertheless, the jet penetration changes would be discussed in detail later in this chapter.

Furthermore, the degree of transverse column flattening (See Figs 3.5 (d-f)) for *Case P1* and *P2* is similar and lower than *Case A*. Indeed, air crossflow spreads the liquid jet along the z direction and smooth the windward surface. Consequently, the instability waves appearing on the windward surface of the jet column are damped out in *Case A* because of the higher viscosity ratio. Referring to tables 2.2 and 2.3, the viscosity ratio in plasma cases is low as the plasma crossflow is more viscous than the air one. Fig 3.7 compares the jet column shape in different conditions and illustrates these variations more clearly. Importantly, when viewed from the top (Figs 3.5 (g-i)), despite the general spray spread being similar in all cases, Fig 3.5 (i) shows less fluid accumulation compared to Fig 3.5 (h).

For each case, three magnified side-view snapshots from a liquid jet breakup are shown in Fig 3.6 to prepare a finer demonstration of differences and similarities among case studies. As the liquid jet proceeds downstream, some of the perturbations formed at the edge of the liquid column are amplified and elongated into ligaments. These ligaments finally break up into a string of droplets.

Although the Weber number of *Case A* and *Case P1* is the same, changes in the liquid breakup details have been observed in the magnified views. Generally, the shape of fluid structures and ligaments has been observed differently by shifting from air crossflow toward plasma crossflow. Figs 3.6 (a-c) focuses on the initial parts of the jet column and surface stripping. It is visible that the shape of the transverse edges responsible for the column stripping mechanism is not similar.

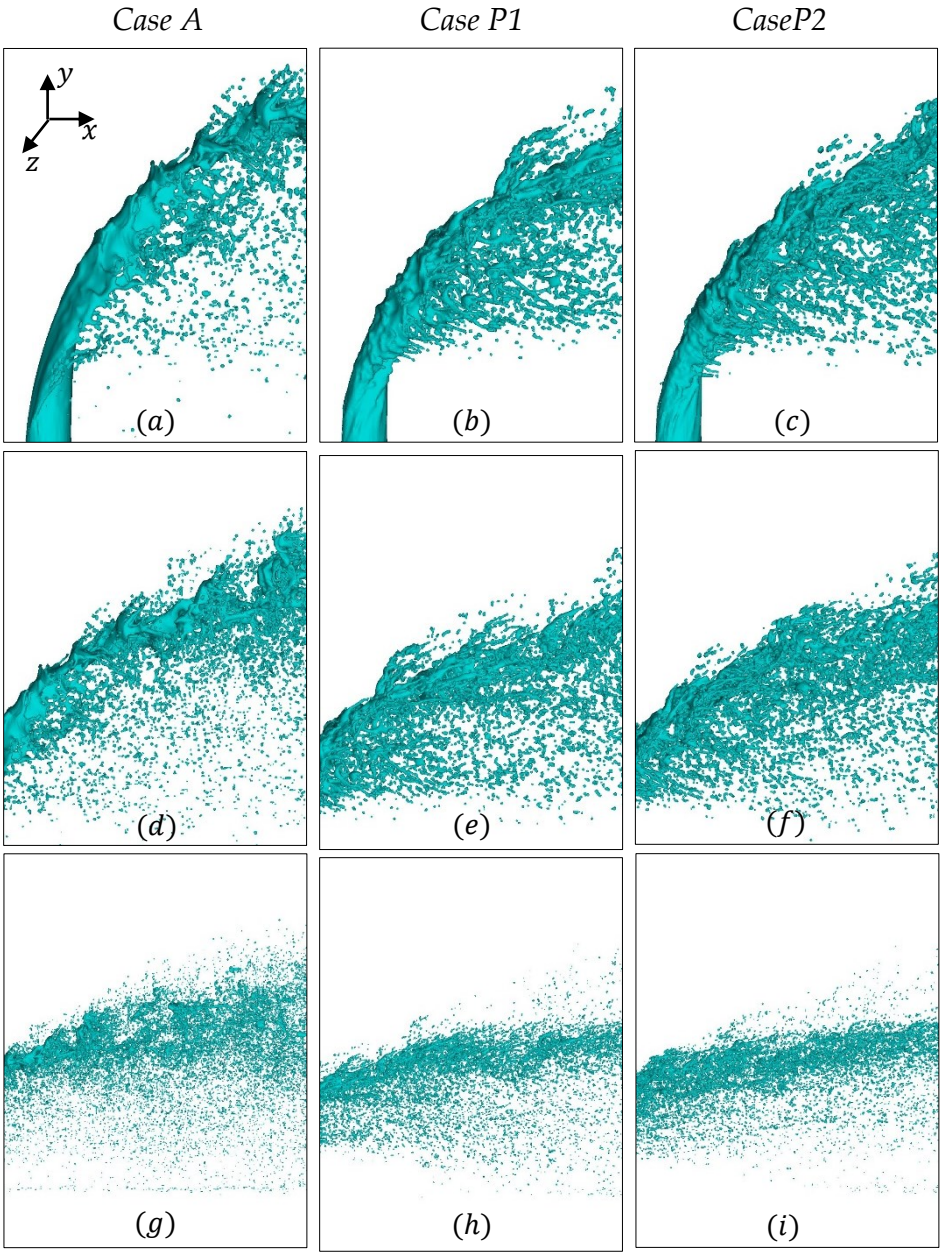

Figure 3.6: Magnified side-view snapshots

Figs 3.6 (d-f) are considering a part of the jet containing column fracture. The difference between the breakup process of *Case A* and *Case P1* is evident. The ligaments and large droplets in *Case P1* and *Case P2* are stretched along the crossflow velocity direction. Definitely, the breakup of liquid jet and ligaments in the near-field affects the size and shape of the droplets in the far-field. Figs 3.6 (g-i) display that in the far-field more droplets are produced in *Case A,* and less accumulation of fluid volume has been occurred. It can indicate that the liquid jet atomization is more severe in this case. Furthermore, the degree of jet bending and liquid breakup does not seem to be sensitive to the increasing We_g from 78 in *Case P1* to 250 in *Case P2*.

Fig 3.7 compares the shape of the jet cross-section at different distances in the y direction to better explain the column deformations. The degree of column flattening has been found similar at $y < d_0$ in all cases. It is visible that at the $y = d_0$ plane, the column stripping has started for *Case A,* and *Case P1* and *Case P2* might show the first signs of stripping. The last plane has chosen at $\frac{y}{d_0} = 5.5$, where the jet column has fractured for cases using plasma crossflow. For $y > d_0$, as the distance to the jet injection orifice increases, the liquid column is more distorted. As mentioned before, the width of the jet column in the transverse z direction is lower in the cases using plasma as crossflow. This result can be seen in Fig. 3.7 for $d_0 < y < 2d_0$, as well.

In addition, the near-field surface waves are different from presenting only on the windward surface in *Case A* to cover the whole circumference of the liquid column at *Case P1* and *Case P2*. (Refer to Figs. 3.7 (d-l) and Figs 3.6 (a-c)). This dissimilarity changes the shape of the jet column edge. According to Fig 3.7, the surface stripping mechanism is more dominant at $\frac{y}{d_0} = 3$ and $\frac{y}{d_0} = 4$ for plasma cases and more droplets are stripped off the liquid column. Indeed, the liquid depletion induced by this breakup mechanism is much dominant in these cases. Fig. 3.7 demonstrates that the depletion of

the liquid column by surface stripping makes the liquid column thinner as the jet penetrates into the crossflow and eventually facilitates jet column breakup. Jet column cross-section at $\frac{y}{d_0} = 5.5$ manifests earlier liquid column fracture in *Case P1* and *P2*. More details about jet penetration and breakup point are presented later.

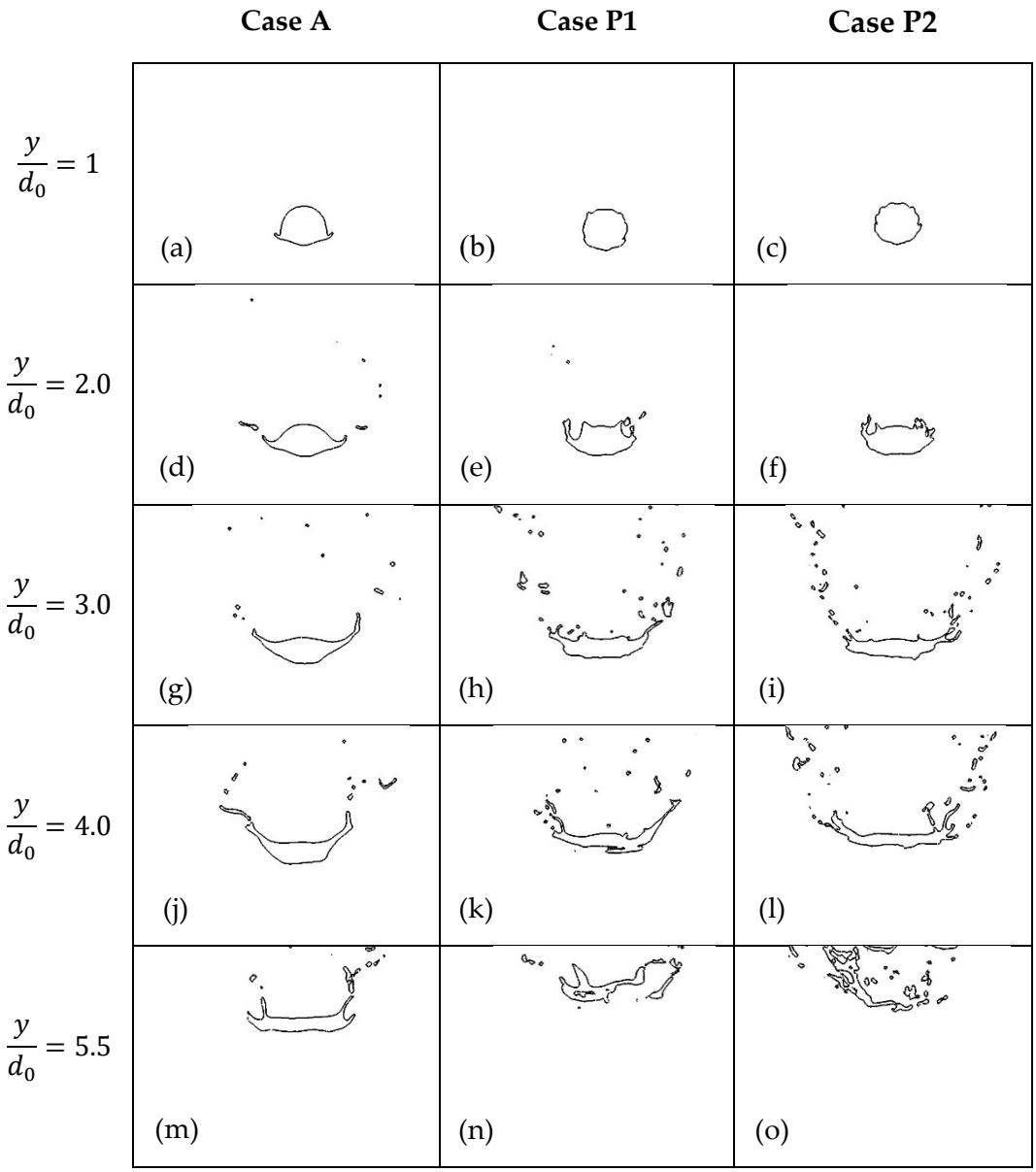

Figure 3.7: Jet column shape at several *xz* plane cross-sections.

3.3 Spray Plume Boundaries

In order to identify isolated blubs, ligaments, and droplets a *tag* function is used. This function considers a unique index for each droplet and provides the location of each of them. The data relating to the positions of the droplets can be extracted quantitatively from the simulation and help provide the spray plume boundaries. In this approach, the x axis is discretized using an equal increment of 0.8 mm. Then, for each x location, the minimum and maximum of the y and z locations of the liquid bulks are identified. The results of the post-processing job have been averaged over fifty time instants along 1 ms. Finally, spray plume boundaries have been obtained and displayed in Fig. 3.8.

It should be noticed that the considerable variation of the data can be occurred due to the small increment size and the small number of samples in it. In addition, the large increment size is not able to capture the local oscillations of the jet boundary. Moreover, it is mentionable that the previous experimental works only acquired the y direction of the jet boundary because of the optical setup restrictions.

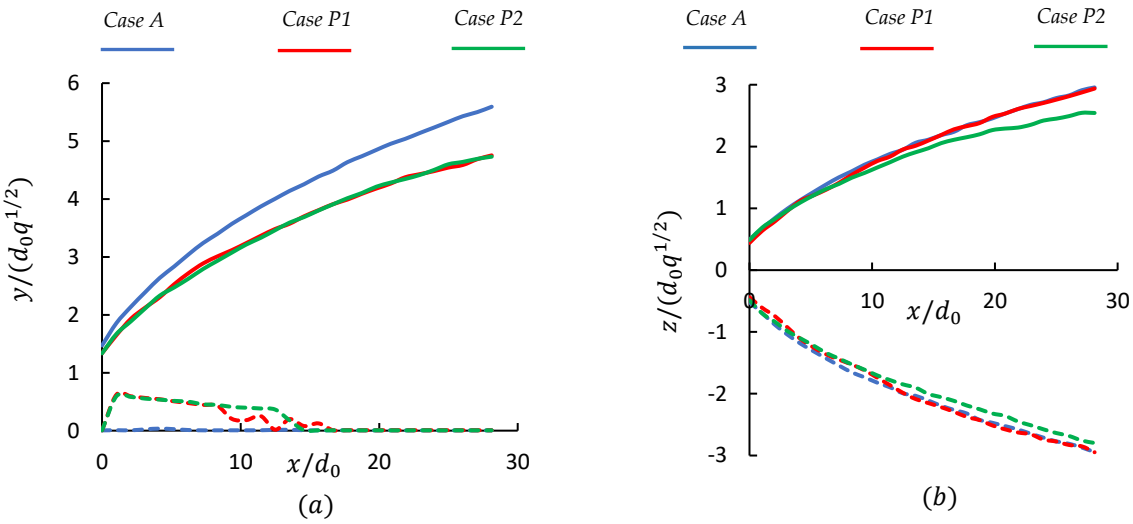

Figure 3.8: Spray plume boundaries for different conditions, (a) xy, and (b) xz plane. Solid and dashed lines represent the maximum and minimum boundaries, respectively.

In Fig. 3.8 (a), using air as a gas crossflow resulted in increasing liquid jet penetration and reducing the minimum of spray boundary in the y direction. It means that in *Case A* there is a delay in jet fracture. These variations can be observed in previous figures, as well. Regarding *Case P1* and *Case P2*, it has been revealed that an increase in We_g, does not have a sensible effect on the degree of jet bending and surface breakup and both cases show similar maximum and minimum spray boundaries in the y direction.

Penetration of the spray plume boundaries in the z direction has been demonstrated in Fig. 3.8 (b). It shows that the trajectories in the near-field and far-field areas are symmetric for all the cases. Generally, the liquid dispersion along the z direction looks the same for different conditions, whereas the droplets stream is more accumulated for *Case P2*. This can be related to the direction of the initial trajectories when liquid ligaments and droplets were separating from the jet column.

3.4 Near-field Breakup Properties

Breakup point location and the length of the instability waves identified on the windward side of the jet column are the breakup properties that can be expressed quantitatively. These properties illustrate the jet fracture process more clearly. The data measuring approach has been explained thoroughly in Section 3.1. Briefly, thin slices of the liquid surface in the xy plane have been obtained for 50 consecutive time steps and the desired properties have been measured by averaging them.

Table 3.2 displays the projection of the liquid column fracture point along the x and y axes and also the length of the instabilities and surface waves that govern the jet breakup. It indicates that the jet column has the most extended height in *Case A* and the length of the instability waves can increase almost 60 percent when using air as a crossflow. The effect of reducing liquid surface tension by switching from *Case P1* to *Case P2* has been demonstrated. Besides, the severe jet column depletion in *Case P2* has

been discussed previously (See Fig. 3.7). This leads to an earlier column breakup which has been certified quantitatively in Table 3.2. The table confirms that higher jet penetration in y direction is caused by the longer length of the instability waves.

Table 3.2: Column breakup locations and wavelength of instabilities

Case	$\frac{x_b}{d_0}$	$\frac{y_b}{d_0}$	$\frac{\lambda}{d_0}$
A	*4.55*	*6.5*	*0.76*
P1	*5.15*	*6.15*	*0.49*
P2	*3.65*	*5.5*	*0.45*

3.4 Droplet Size Distribution

One of the applications of the *tag* function is providing the volume and consequently the mass of each liquid chunk. In this manner, the impact of different conditions on the droplet statistics can be analyzed by extracting the droplets' size in the form of probability density functions (PDFs). The PDFs indicate the sensitivity of the droplets' size to the jet atomization conditions. Fig. 3.9 compares the PDFs of the droplets at different sizes.

It should be mentioned that the number of droplets is obtained in a steady-state condition. For *Case A, P1* and *P2,* it took respectively around 5, 12 and 8 ms to achieve this condition, where the mass of the injected liquid is conserved during the atomization and equal to the outlet mass. To rephrase it, after these temporal values, the number of the produced liquid chunks is constant due to its variation being small and negligible. As mentioned in the previous chapter, the minimum cell size of the simulation is $\Delta x_{min} = 22.9\ \mu m$. In this section, the discovered droplets with a diameter

smaller than $2 * \Delta x_{min}$ are not considered fully resolved and are removed to stabilize the results. Therefore, the smallest reported droplet has a diameter of $0.46\,\mu m$. The following results are insensitive to this consideration, as the size and mass of the removed droplets are small.

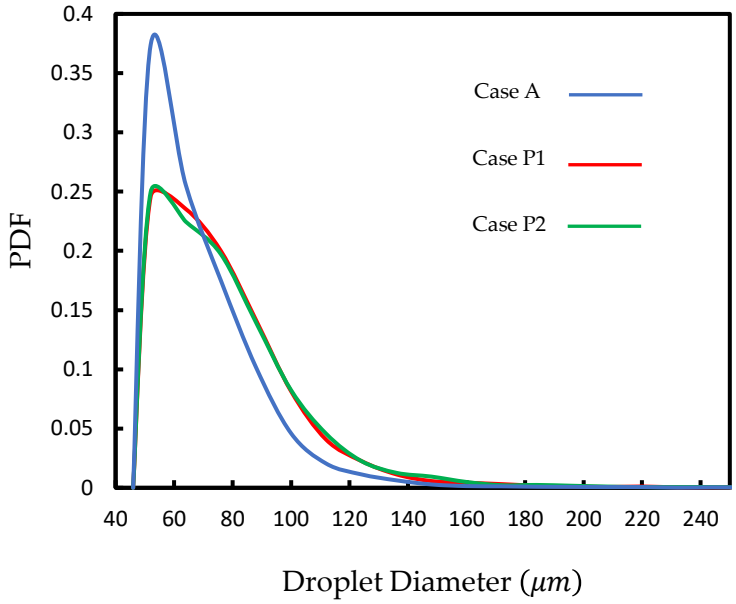

(a)

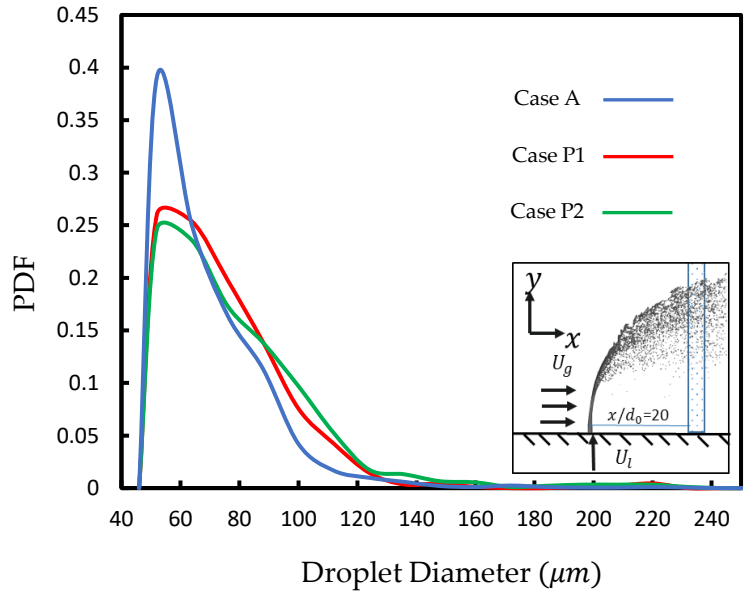

(b)

Figure 3.9: Size distribution of droplets collected: (a) at the entire domain, (b) inside a yz plane at $\frac{x}{d_0} = 20$.

In Fig. 3.9 (a), all the droplets in the entire domain have been studied, while Fig. 3.9 (b) considers only the droplets collected at the far-field between planes $\frac{x}{d_0} = 20$ and $\frac{x}{d_0} = 21$. It is noticeable that the total number of the discovered droplets for *Case P2* is slightly higher than *Case P1* and almost half of the droplets in *Case A*.

As demonstrated in Fig. 3.9 (a), the size of the droplets presents a unimodal distribution which gradually declines toward larger droplets. It shows that for all cases, many of the droplets have a diameter less than $80\mu m$. It is obtained that not only the number of the droplets generated in *Case A* is higher, but also the size of them is smaller. This clearly shows a higher degree of liquid atomization happening in this case. Moreover, the effect of switching We_g between *Case P1* and *Case P2* has been observed unimportant in the distribution of the droplet sizes. This result is expected as their liquid column breakup founded qualitatively similar. Nevertheless, the number of the generated droplets in *Case P2* is almost 10 percent higher compared with *Case P1*, as the surface tension is lower.

To learn more about the droplets' sizes at the far-field, the droplets located between planes $\frac{x}{d_0} = 20$ and $\frac{x}{d_0} = 21$ have been investigated. Fig 3.9 (b) displays that the presence of the larger droplets is more dominant in *Case P2* than *Case P1.* As the examined yz plane is a sub-domain of the entire domain, the trend of the displayed graphs in this figure is similar to their counterparts in Fig 3.9 (a).

Chapter 4

Conclusions and Future Work

The main scope of this study was the numerical simulation of the LJIC involved in SPS coating process. On this subject, the primary parameters controlling liquid jet breakup in a plasma crossflow have been calculated and shaped two case studies. In addition, another case study representing the LJIC in a wind tunnel has been considered. The primary parameters of the latter case are like the plasma ones as far as possible. Finally, the results provided a functional and advanced comprehension of the LJIC mechanism engaged in SPS techniques.

4.1 Conclusions

- Although a remarkable change has not been observed in the jet penetration height, the jet bending degree of the jets injected in the plasma crossflow has been realized slightly higher than air one resulting in a higher jet height in wind tunnel atmospheric conditions.
- Liquid jet depletion originated by the surface stripping mechanism diminishes the thickness of the flattened jet column and facilitates the column fracture. This

phenomenon has been found more severe where the surface tension is lower. Typically, the starting point of the column stripping is observed at $y = d_0$ plane for all cases.

- Generally, the shape of the fluid structure and generated ligaments would be extended along the crossflow direction when a liquid jet is injected into the plasma crossflow.
- When it comes to the atmospheric condition, the windward surface of the jet column is smoother and the instability waves are encountered with an increase in their length. Indeed, the longer waves, the liquid jet penetrates more into the crossflow.
- Even though the entire circumference of the jet is engaged with the surface waves in SPS techniques, these waves have been detected only on the windward surface when doing tests in the wind tunnel. This led to more severe liquid depletion in the mentioned methods.
- Dealing with the distribution of the droplet sizes, many of the droplets have a diameter lower than $80\mu m$. Also, the liquid injection into the wind tunnel produced more droplets with smaller sizes than injection in plasma crossflow. Therefore, it can be concluded that the degree of the liquid atomization is lower in the latter cases. In general, the droplet size distribution in the entire domain has not been found sensitive to the change of liquid characteristics such as surface tension. Nonetheless, the presence of larger droplets in the far-field is more dominant by increasing We_g.

4.2 Scope for Future Work

In this section, some scopes are presented for future works in LJIC in SPS. It must be mentioned out that the implemented numerical method and AMR technique have been

found capable in high fidelity simulation of LJIC. In other words, using the applied numerical solver (Basilisk) coupled with high-performance computing and software developing skills, one can provide detailed prediction and analysis of the spray atomization process.

- The gaseous flow distribution similar to the actual plasma jet near the liquid column may be considered. The gaseous flow investigation is useful in indicating the low-pressure zone behind the jet, and features of the vortices affect the shape of the jet column cross-sections and fracture.
- Considering the most prominent features of the obtained high-resolution Spatio-temporal data is of interest. This is the concept of reduced-order modeling (ROM) techniques such as proper orthogonal decomposition (POD) that is useful for analyzing the liquid jet dynamics.
- Most of the numerical studies of SPS and/or SPPS have been employed Taylor Analogy Breakup (TAB) or Kelvin-Helmholtz Rayleigh-Taylor (KHRT) breakup models. The results of these models are affected by several constants. One can use the values obtained in this study for the constants of the mentioned models.
- There are various parameters involved in the SPS process, such as plasma arc fluctuations. The effect of these fluctuations on the jet breakup physics can provide more profound knowledge by the implemented numerical approach.

Bibliography

[1] N. Chigier and R. D. Reitz, "Regimes of jet breakup and breakup mechanisms-Physical aspects," *Recent Adv. spray Combust. Spray At. drop Burn. phenomena.*, vol. 1, pp. 109–135, 1996.

[2] K. A. Sallam, C. Ng, and R. Sankarakrishnan, "Breakup of Turbulent and Non-Turbulent Liquid jets in Gaseous Crossflows," no. March, 2015, doi: 10.2514/6.2006-1517.

[3] Y. Jiang, H. Li, L. Hua, D. Zhang, and Z. Issaka, "Experimental Study on Jet Breakup Morphologies and Jet Characteristic Parameters of Non-circular Nozzles under Low-intermediate Pressures," *Appl. Eng. Agric.*, vol. 35, no. 4, pp. 617–632, 2019, doi: https://doi.org/10.13031/aea.13291.

[4] D. Sedarsky *et al.*, "Model validation image data for breakup of a liquid jet in crossflow: Part i," *Exp. Fluids*, vol. 49, no. 2, pp. 391–408, Aug. 2010, doi: 10.1007/s00348-009-0807-2.

[5] K. A. Sallam, C. Aalburg, and G. M. Faeth, "Breakup of round nonturbulent liquid jets in gaseous crossflow," *AIAA J.*, vol. 42, no. 12, pp. 2529–2540, 2004, doi: 10.2514/1.3749.

[6] J. N. Stenzler, J. G. Lee, D. A. Santavicca, and W. Lee, "PENETRATION OF LIQUID JETS IN A CROSS-FLOW," vol. 16, pp. 887–906, 2006.

[7] S. Ghods, "Detailed Numerical Simulation of Liquid Jet In Crossflow Atomization with High Density Ratios," *ProQuest Diss. Theses*, no. August, p. 98, 2013, [Online]. Available:

https://search.proquest.com/docview/1418021493?accountid=7181%5Cnhttp://yg5km5gl9x.search.serialssolutions.com/?ctx_ver=Z39.88-2004&ctx_enc=info:ofi/enc:UTF-8&rfr_id=info:sid/ProQuest+Dissertations+%26+Theses+Global&rft_val_fmt=info:ofi/fmt:kev:mtx:disser.

[8] E. Farvardin, "Biodiesel Spray Characterization: A Combined Numerical and Experimental Analysis," Concordia University, 2013.

[9] M. Jadidi, S. Moghtadernejad, and A. Dolatabadi, "Penetration and breakup of liquid jet in transverse free air jet with application in suspension-solution thermal sprays," *Mater. Des.*, vol. 110, pp. 425–435, 2016.

[10] J. R. Davis, *Handbook of thermal spray technology*. 2004.

[11] E. Lugscheider, C. Barimani, P. Eckert, and U. Eritt, "Modeling of the APS plasma spray process," *Comput. Mater. Sci.*, vol. 7, no. 1–2, pp. 109–114, Dec. 1996, doi: 10.1016/S0927-0256(96)00068-7.

[12] V. Viswanathan, T. Laha, K. Balani, A. Agarwal, and S. Seal, "Challenges and advances in nanocomposite processing techniques," *Mater. Sci. Eng. R Reports*, vol. 54, no. 5–6, pp. 121–285, 2006, doi: 10.1016/j.mser.2006.11.002.

[13] R. Vaen, H. Kaner, G. Mauer, and D. Stöver, "Suspension plasma spraying: Process characteristics and applications," in *Journal of Thermal Spray Technology*, Jan. 2010, vol. 19, no. 1–2, pp. 219–225, doi: 10.1007/s11666-009-9451-x.

[14] C. Marchand, C. Chazelas, G. Mariaux, and A. Vardelle, "Liquid precursor plasma spraying: Modeling the interactions between the transient plasma jet and the droplets," *J. Therm. Spray Technol.*, vol. 16, no. 5–6, pp. 705–712, 2007, doi:

10.1007/s11666-007-9112-x.

[15] E. Meillot, S. Vincent, C. Caruyer, D. Damiani, and J. P. Caltagirone, "Modelling the interactions between a thermal plasma flow and a continuous liquid jet in a suspension spraying process," *J. Phys. D. Appl. Phys.*, vol. 46, no. 22, 2013, doi: 10.1088/0022-3727/46/22/224017.

[16] M. Jadidi, M. Mousavi, S. Moghtadernejad, and A. Dolatabadi, "A Three-Dimensional Analysis of the Suspension Plasma Spray Impinging on a Flat Substrate," *J. Therm. Spray Technol.*, vol. 24, no. 1, pp. 11–23, 2015, doi: 10.1007/s11666-014-0166-2.

[17] P. Fauchais, G. Montavon, R. S. Lima, and B. R. Marple, "Engineering a new class of thermal spray nano-based microstructures from agglomerated nanostructured particles, suspensions and solutions: An invited review," *Journal of Physics D: Applied Physics*, vol. 44, no. 9. Mar. 09, 2011, doi: 10.1088/0022-3727/44/9/093001.

[18] E. Meillot, R. Vert, C. Caruyer, D. Damiani, and M. Vardelle, "Manufacturing nanostructured YSZ coatings by suspension plasma spraying (SPS): Effect of injection parameters," *J. Phys. D. Appl. Phys.*, vol. 44, no. 19, May 2011, doi: 10.1088/0022-3727/44/19/194008.

[19] F. Jabbari, M. Jadidi, R. Wuthrich, and A. Dolatabadi, "A Numerical Study of Suspension Injection in Plasma-Spraying Process," *J. Therm. Spray Technol.*, vol. 23, no. 1–2, pp. 3–13, Jan. 2014, doi: 10.1007/s11666-013-0030-9.

[20] J. Fazilleau, C. Delbos, V. Rat, J. F. Coudert, P. Fauchais, and B. Pateyron, "Phenomena involved in suspension plasma apraying part 1: Suspension injection and behavior," *Plasma Chem. Plasma Process.*, 2006, doi: 10.1007/s11090-006-9019-1.

[21] D. Damiani, D. Tarlet, and E. Meillot, "A Particle-Tracking-Velocimetry (PTV) Investigation of Liquid Injection in a DC Plasma Jet," *J. Therm. Spray Technol.*, vol. 23, no. 3, pp. 340–353, 2014, doi: 10.1007/s11666-013-0050-5.

[22] K. Pourang, C. Moreau, and A. Dolatabadi, "Effect of Substrate and Its Shape on in-Flight Particle Characteristics in Suspension Plasma Spraying," *J. Therm. Spray Technol.*, vol. 25, no. 1, pp. 44–54, 2016, doi: 10.1007/s11666-015-0342-z.

[23] E. Dalir, A. Dolatabadi, and J. Mostaghimi, "Modeling the effect of droplet shape and solid concentration on the suspension plasma spraying," *Int. J. Heat Mass Transf.*, vol. 161, p. 120317, 2020, doi: 10.1016/j.ijheatmasstransfer.2020.120317.

[24] E. Dalir, A. Dolatabadi, and J. Mostaghimi, "Modeling of Suspension Plasma Spraying Process Including Arc Movement Inside the Torch," *J. Therm. Spray Technol.*, vol. 28, no. 6, pp. 1105–1125, 2019.

[25] J. F. Bisson, C. Moreau, M. Dorfman, C. Dambra, and J. Mallon, "Influence of hydrogen on the microstructure of plasma-sprayed yttria-stabilized zirconia coatings," *J. Therm. Spray Technol.*, vol. 14, no. 1, pp. 85–90, 2005, doi: 10.1361/10599630522422.

[26] K. A. Sallam, C. Aalburg, and G. M. Faeth, "Breakup of round nonturbulent liquid jets in gaseous crossflow," *AIAA J.*, vol. 42, no. 12, pp. 2529–2540, 2004.

[27] G. M. Mazallon, J; Dai, Z; Faeth, "Primary Breakup of Nonturbulent Liquid Jets in Gas Crossflows," *At. Sprays*, vol. 9, pp. 291–311, 1999.

[28] C. Ng, R. Sankarakrishnan, and K. A. Sallam, "Bag breakup of nonturbulent liquid jets in crossflow," vol. 34, pp. 241–259, 2008, doi: 10.1016/j.ijmultiphaseflow.2007.07.005.

[29] G. Vich and M. Ledoux, "Investigation of a Liquid Jet in a Subsonic Cross-Flow," *Int. J. Fluid Mech. Res.*, vol. 24, pp. 1–12, 1997.

[30] M. Birouk, B. J. Azzopardi, and T. St, "Primary Break-up of a Viscous Liquid Jet in a Cross Airflow," vol. 20, no. March, 2003.

[31] E. Farvardin, M. Johnson, R. Canada, H. Alaee, A. Martinez, and A. Dolatabadi, "Comparative Study of Biodiesel and Diesel Jets in Gaseous," vol. 29, no. 6, 2013, doi: 10.2514/1.B34743.

[32] P. Wu, K. A. Kirkendall, R. P. Fuller, U. S. A. Force, W. Patterson, and A. Force, "Breakup Processes of Liquid Jets in Subsonic Cross ows," vol. 13, no. 1, 1997, doi: 10.2514/2.5151.

[33] K. Lee and C. Aalburg, "Primary Breakup of Turbulent Round Liquid Jets in Uniform Cross fl ows," vol. 45, no. 8, 2007, doi: 10.2514/1.19397.

[34] C. Aalburg, "Primary Breakup of Round Turbulent Liquid Jets in Uniform Crossflows," no. January, pp. 1–12, 2005.

[35] A. R. Osta and K. A. Sallam, "Nozzle-Geometry Effects on Upwind-Surface Properties of Turbulent Liquid Jets in Gaseous Cross fl ow," vol. 26, no. 5, 2010, doi: 10.2514/1.49737.

[36] L. Xie, X. Ma, E. H. Jordan, N. P. Padture, D. T. Xiao, and M. Gell, "Deposition of thermal barrier coatings using the solution precursor plasma spray process," *J. Mater. Sci.*, vol. 39, no. 5, pp. 1639–1646, 2004, doi: 10.1023/B:JMSC.0000016163.81534.19.

[37] S. Vincent, G. Balmigere, C. Caruyer, E. Meillot, and J. P. Caltagirone, "Contribution to the modeling of the interaction between a plasma flow and a

liquid jet," *Surf. Coatings Technol.*, vol. 203, no. 15, pp. 2162–2171, 2009, doi: 10.1016/j.surfcoat.2008.11.009.

[38] C. Marchand, A. Vardelle, G. Mariaux, and P. Lefort, "Modelling of the plasma spray process with liquid feedstock injection," *Surf. Coatings Technol.*, vol. 202, no. 18, pp. 4458–4464, 2008, doi: 10.1016/j.surfcoat.2008.04.027.

[39] C. Caruyer, S. Vincent, E. Meillot, and J. P. Caltagirone, "Modeling the first instant of the interaction between a liquid and a plasma jet with a compressible approach," *Surf. Coatings Technol.*, vol. 205, no. 4, pp. 974–979, 2010, doi: 10.1016/j.surfcoat.2010.07.073.

[40] S. Vincent, G. Balmigère, J. Caltagirone, and E. Meillot, "Eulerian – Lagrangian multiscale methods for solving scalar equations – Application to incompressible two-phase flows," *J. Comput. Phys.*, vol. 229, no. 1, pp. 73–106, 2010, doi: 10.1016/j.jcp.2009.09.007.

[41] E. Meillot, S. Vincent, C. Caruyer, J. P. Caltagirone, and D. Damiani, "From DC time-dependent thermal plasma generation to suspension plasma-spraying interactions," *J. Therm. Spray Technol.*, vol. 18, no. 5–6, pp. 875–886, 2009, doi: 10.1007/s11666-009-9354-x.

[42] E. Meillot, D. Damiani, S. Vincent, C. Caruyer, and J. P. Caltagirone, "Analysis by modeling of plasma flow interactions with liquid injection," *Surf. Coat. Technol.*, vol. 220, pp. 149–156, 2013, doi: 10.1016/j.surfcoat.2012.11.025.

[43] Y. Shan, T. W. Coyle, and J. Mostaghimi, "Modeling the influence of injection modes on the evolution of solution sprays in a plasma jet," *J. Therm. Spray Technol.*, vol. 19, no. 1–2, pp. 248–254, 2010, doi: 10.1007/s11666-009-9434-y.

[44] E. Dalir, C. Moreau, and A. Dolatabadi, "Three-Dimensional Modeling of Suspension Plasma Spraying with Arc Voltage Fluctuations," *Journal of Thermal Spray Technology*, vol. 27, no. 8. pp. 1465–1490, 2018, doi: 10.1007/s11666-018-0783-2.

[45] A. Farrokhpanah, T. W. Coyle, and J. Mostaghimi, "Numerical Study of Suspension Plasma Spraying," *J. Therm. Spray Technol.*, vol. 26, no. 1, pp. 12–36, 2017, doi: 10.1007/s11666-016-0502-9.

[46] H. Xiong and W. Sun, "Investigation of Droplet Atomization and Evaporation in Solution Precursor Plasma Spray Coating," *Coatings*, vol. 7, no. 11, 2017, doi: 10.3390/coatings7110207.

[47] S. Popinet, S. P. Quadtree-adaptive, and S. Verlag, "Quadtree-adaptive tsunami modelling To cite this version : HAL Id : hal-01445423 Quadtree-adaptive tsunami modelling," vol. 61, no. 9, pp. 1261–1285, 2017.

[48] D. Fuster, G. Agbaglah, C. Josserand, S. Popinet, and S. Zaleski, "Numerical simulation of droplets, bubbles and waves: State of the art," *Fluid Dyn. Res.*, vol. 41, no. 6, 2009, doi: 10.1088/0169-5983/41/6/065001.

[49] C. Josserand and S. Zaleski, "Droplet splashing on a thin liquid film," *Phys. Fluids*, vol. 15, no. 6, pp. 1650–1657, 2003, doi: 10.1063/1.1572815.

[50] S. Popinet, "Gerris: A tree-based adaptive solver for the incompressible Euler equations in complex geometries," *J. Comput. Phys.*, vol. 190, no. 2, pp. 572–600, 2003, doi: 10.1016/S0021-9991(03)00298-5.

[51] D. Fuster and S. Popinet, "An all-Mach method for the simulation of bubble dynamics problems in the presence of surface tension," *J. Comput. Phys.*, vol. 374,

pp. 752–768, 2018.

[52] B. Zhang, S. Popinet, and Y. Ling, "Modeling and detailed numerical simulation of the primary breakup of a gasoline surrogate jet under non-evaporative operating conditions," *Int. J. Multiph. Flow*, vol. 130, 2020, doi: 10.1016/j.ijmultiphaseflow.2020.103362.

[53] R. Scardovelli and S. Zaleski, "Direct numerical simulation of free-surface and interfacial flow," *Annu. Rev. Fluid Mech.*, vol. 31, no. May, pp. 567–603, 1999, doi: 10.1146/annurev.fluid.31.1.567.

[54] E. Aulisa, S. Manservisi, R. Scardovelli, and S. Zaleski, "Interface reconstruction with least-squares fit and split advection in three-dimensional Cartesian geometry," *J. Comput. Phys.*, vol. 225, no. 2, pp. 2301–2319, 2007.

[55] R. Scardovelli and S. Zaleski, "Analytical relations connecting linear interfaces and volume fractions in rectangular grids," *J. Comput. Phys.*, vol. 164, no. 1, pp. 228–237, 2000.

[56] M. M. Francois, S. J. Cummins, E. D. Dendy, D. B. Kothe, J. M. Sicilian, and M. W. Williams, "A balanced-force algorithm for continuous and sharp interfacial surface tension models within a volume tracking framework," *J. Comput. Phys.*, vol. 213, no. 1, pp. 141–173, 2006, doi: 10.1016/j.jcp.2005.08.004.

[57] S. Popinet, "An accurate adaptive solver for surface-tension-driven interfacial flows," *J. Comput. Phys.*, vol. 228, no. 16, pp. 5838–5866, 2009.

[58] A. Brandt, "Guide to multigrid development," in *Multigrid methods*, Springer, 1982, pp. 220–312.

[59] J. B. Bell, P. Colella, and H. M. Glaz, "A second-order projection method for the

incompressible Navier-Stokes equations," *J. Comput. Phys.*, vol. 85, no. 2, pp. 257–283, 1989.

[60] S. Popinet, "Basilisk Code." http://basilisk.fr/Front Page.

[61] W. J. Coirier, "An adaptively-refined, Cartesian, cell-based scheme for the Euler and Navier-Stokes equations," 1994.

[62] L. H. Howell and J. B. Bell, "An adaptive mesh projection method for viscous incompressible flow," *SIAM J. Sci. Comput.*, vol. 18, no. 4, pp. 996–1013, 1997, doi: 10.1137/S1064827594270555.

[63] M. J. Berger and J. Oliger, "Adaptive mesh refinement for hyperbolic partial differential equations," *J. Comput. Phys.*, vol. 53, no. 3, pp. 484–512, 1984, doi: https://doi.org/10.1016/0021-9991(84)90073-1.

[64] A. M. Khokhlov, "Fully Threaded Tree Algorithms for Adaptive Refinement Fluid Dynamics Simulations," *J. Comput. Phys.*, vol. 143, no. 2, pp. 519–543, Jul. 1998, doi: 10.1006/JCPH.1998.9998.

[65] A. Almgren, J. Bell, and W. Szymczak, "A Numerical Method for the Incompressible Navier-Stokes Equations Based on an Approximate Projection," *SIAM J. Sci. Comput.*, vol. 17, pp. 358–369, 1996.

[66] M. L. Minion, "A projection method for locally refined grids," *J. Comput. Phys.*, vol. 127, no. 1, pp. 158–178, 1996, [Online]. Available: http://inis.iaea.org/search/search.aspx?orig_q=RN:28049975.

[67] W. Hackbusch, *Multi-grid methods and applications*, vol. 4. Springer Science & Business Media, 2013.

[68] S. Popinet, "A quadtree-adaptive multigrid solver for the Serre–Green–Naghdi equations," *J. Comput. Phys.*, vol. 302, pp. 336–358, 2015, doi: https://doi.org/10.1016/j.jcp.2015.09.009.

[69] Y. Ling, G. Legros, S. Popinet, and S. Zaleski, "Direct numerical simulation of an atomizing biodiesel jet: Impact of fuel properties on atomization characteristics," *ILASS-Europe, 28th Conf. Liq. At. Spray Syst.*, doi: 10.4995/ilass2017.2017.5035.

[70] J. A. van Hooft, S. Popinet, C. C. van Heerwaarden, S. J. A. van der Linden, S. R. de Roode, and B. J. H. van de Wiel, "Towards Adaptive Grids for Atmospheric Boundary-Layer Simulations," *Boundary-Layer Meteorol.*, vol. 167, no. 3, pp. 421–443, 2018, doi: 10.1007/s10546-018-0335-9.

[71] S. Popinet, "Quadtree-adaptive tsunami modelling," *Ocean Dyn.*, vol. 61, no. 9, pp. 1261–1285, 2011, doi: 10.1007/s10236-011-0438-z.

[72] M. Griebel and G. Zumbusch, "Hash based adaptive parallel multilevel methods with space-filling curves," *NIC Symp.*, vol. 9, pp. 3–00, 2001, [Online]. Available: http://scholar.google.com/scholar?hl=en&btnG=Search&q=intitle:Hash+Based+Adaptive+Parallel+Multilevel+Methods+with+Space-Filling+Curves#0.

[73] Y. P. Wan, S. Sampath, V. Prasad, R. Williamson, and J. R. Fincke, "An advanced model for plasma spraying of functionally graded materials," *J. Mater. Process. Technol.*, vol. 137, no. 1-3 SPEC, pp. 110–116, 2003, doi: 10.1016/S0924-0136(02)01096-8.

[74] X. Sun and J. Heberlein, "Fluid dynamic effects on plasma torch anode erosion," *J. Therm. Spray Technol.*, vol. 14, pp. 39–44, 2005, doi: 10.1361/10599630522404.

[75] X. Li and M. C. Soteriou, "High fidelity simulation and analysis of liquid jet

atomization in a gaseous crossflow at intermediate Weber numbers," *Phys. Fluids*, vol. 28, no. 8, pp. 2101–2135, 2016.

[76] X. Li and M. C. Soteriou, "High fidelity simulation and analysis of liquid jet atomization in a gaseous crossflow at intermediate weber numbers," *Phys. Fluids*, vol. 28, no. 8, 2016, doi: 10.1063/1.4959290.

[77] J. Song, C. Cain, and J. Lee, "Liquid Jets in Subsonic Air Crossflow at Elevated Pressure," *J. Eng. Gas Turbines Power*, vol. 137, 2015, doi: 10.1115/1.4028565.

[78] X. Li and M. C. Soteriou, "Detailed numerical simulation of liquid jet atomization in crossflow of increasing density," *Int. J. Multiph. Flow*, vol. 104, pp. 214–232, 2018, doi: 10.1016/j.ijmultiphaseflow.2018.02.016.